


Article

Origin of the Granite Porphyry and Related Xiajinbao Au Deposit at Pingquan, Hebei Province, Northeastern China: Constraints from Geochronology, Geochemistry, and H–O–S–Pb–Hf Isotopes

Qingquan Liu ^{1,2,3} , Yongjun Shao ^{2,3}, Zhongfa Liu ^{2,3}, Jianguo Zhang ^{2,3,4}
and Cheng Wang ^{2,3,*}

¹ School of Resources and Safety Engineering, Central South University, Changsha 410083, China; liuqingquan@csu.edu.cn

² Key Laboratory of Metallogenic Prediction of Non-Ferrous Metals and Geological Environment Monitoring, Central South University, Ministry of Education, Changsha 410083, China; shaoyongjun@126.com (Y.S.); liuzf61521@csu.edu.cn (Z.L.); zjglove@126.com (J.Z.)

³ School of Geosciences and Info-Physics, Central South University, Changsha 410083, China

⁴ China Non-Ferrous Metals Geological Survey, Beijing 100012, China

* Correspondence: csuwangcheng@csu.edu.cn; Tel.: +86-731-888-30616

Received: 13 June 2018; Accepted: 26 July 2018; Published: 31 July 2018



Abstract: The Xiajinbao gold deposit is a medium-sized gold deposit in the Jidong gold province. Ore bodies mainly occur within the Xiajinbao granite porphyry and along the contact zone between the intrusion and Archean plagioclase hornblende gneiss. The zircon LA-ICP-MS age of the Xiajinbao granite porphyry yields 157.8 ± 3.4 Ma, which reflects the metallogenic age of the gold mineralization. Its petrographic features, major and trace element contents, zircon Hf isotopic model ages and compositional features all demonstrate that the Xiajinbao granitic magma is derived from partial melting of the Changcheng unit. The results of H–O isotopic analyses of auriferous quartz veins indicate that the ore-forming fluids are derived from magmatic waters that gradually mixed with meteoric waters during the evolution of the ore-forming fluids. S–Pb isotopic data indicate that the ore-forming fluids were mainly provided by the magma and by plagioclase hornblende gneisses. The gold metallogeny of the Xiajinbao gold deposit is temporally, spatially, and genetically associated with the high-K calc-alkaline-shoshonitic granitic magma emplaced during the Yanshanian orogeny and intruding the Archean plagioclase hornblende gneisses. These magmatic events mainly occurred during the period of 223–153 Ma and comprise three peak periods in the late Triassic (225–205 Ma), the early Jurassic (200–185 Ma) and the middle–late Jurassic (175–160 Ma), respectively. The metallogenic events in this area mainly occurred during the period of 223–155 Ma with the peak periods during the late Triassic (223–210 Ma) and the middle–late Jurassic (175–155 Ma), respectively. Both mineralization and magmatism occurred in a post-collisional tectonic setting related to the collision between the Mongolian plate and the North China plate at the end of the Permian. The magmatism of the early Jurassic occurred during the collision between the Siberian plate and the Mongolian plate, which caused the thickening and melting of the northern margin of the North China plate. The middle and late Jurassic magmatism and metallogenic activities are products of crustal thickening and partial melting during the Yanshanian intra-continental orogeny at the northern margin of the North China plate.

Keywords: geochronology; geochemistry; H–O–S–Pb–Hf isotopes; ore genesis; Xiajinbao Au deposits; Jidong gold province

1. Introduction

More than 70% of China's gold resources occur along the margins of the North China Craton (NCC) and in adjacent orogenic belts [1]. These include China's most important gold deposits of the Jiaodong Peninsula, which is located along the eastern side of the NCC, and the Daqingshan, Yan-Liao, and Changbaishan gold provinces, which are located along the northern margin of the NCC [1]. In the Yan-Liao gold field, there is an EW-trending gold province which yielded about 1000 t of gold [1]. Recent studies reveal that the gold deposits in the NCC formed as a result of multiple orogenic events [2]. Approximately 70% of the gold deposits in the Yan-Liao gold field are hosted by Precambrian metamorphic rocks, while 30% of the gold deposits occur in Paleozoic and Mesozoic intrusive rocks [3]. The Jidong gold province (or eastern Hebei Province; Easting 117°30'–119°00', Northing 40°00'–40°40') belongs to the Yan-Liao gold field. Tectonically, this area is located at the SE margin of the Yanshanian tectonic belt, and at the northern part of the North China plate (Figure 1a). In total, 29 gold deposits and 118 gold occurrences are documented in this area, with an accumulated proven gold reserve of 129.5 tons, which constitutes 2.4% of China's total gold reserves [4]. The economically viable gold deposits in the Jidong area all occur within Mesozoic units and are spatially linked to the intruding felsic intrusions [5], including the large Yuerya gold deposit (Au: 50 t), the large Jinchangyu gold deposit (Au: 10 t), and the medium Huajian (or Niuxinshan) gold deposit (Au: 10 t), Dongliang gold deposit (Au: 19.53 t), Tangzhangzi gold deposit (Au: 1.025 t; Ag: 1 t; Mo: 47 t) and Xiajinbao gold deposit (Au: 3.9 t), respectively (Figure 1b).

The Xiajinbao gold deposit is an important gold deposit located in the Jidong area at the northern margin of the NCC, with an approximate grade of 1.91 g/t. The fission track dating of zircon and apatite reveal that the metallogenic age is about 153.9 Ma [6], which is close to the molybdenite Re–Os model age (163.4 Ma, [7]). The molybdenite Re–Os model age is close to the upper limit of gold mineralization in Xiajinbao deposit. The ore-forming fluid is characterized by moderate–high temperatures and moderate–high salinities, and it is enriched in CO₂ [8]. Previous studies suggest that the Xiajinbao gold deposit represents a porphyry-style gold deposit [7–10]. However, further study of the Xiajinbao Au deposit is required to properly constrain the origin of the Au mineralization and the temporal relationships between mineralization and magmatism, as well as the tectonic setting of this deposit.

In this paper, we present geochemical data, zircon U–Pb age, Hf isotopic compositions and H–O–S–Pb isotopes of the deposit; we discuss the magmatic evolution, the source of the magma and ore-forming fluids, and the geodynamic setting. Based on our new data and in the context of published data, this paper attempts to elucidate the geodynamic setting and hydrothermal evolution of this Mesozoic gold deposit, and we establish a Mesozoic gold metallogenic model.

2. Regional Geology

The Jidong area is an important gold mining province in China. Located at the southeastern part of the Yanshanian tectonic belt (Figure 1b,c) along the northern margin of the North China block, the Jidong area sits at the junction between the North China block, the Siberian plate and the Pacific plate [11]. This area has experienced several tectonic events between 3800 Ma and 1600 Ma [12,13]. During the Mesozoic, the area experienced extensive magmatic activity and related gold, molybdenum, copper, lead, zinc, silver mineralization [14,15].

Widespread Precambrian rocks host most of the gold mineralization in this region, including the Jinchangyu, Yuerya, Huajian, and Dongliang Au deposits. The early Precambrian units consist of metamorphic gneisses that are dated at ca. 3.5 Ga [16,17]. The gneisses include the Paleo- to Mesoarchean Qianxi and Zunhua groups, which consist of granulite- to amphibolite-facies ortho- and paragneisses, as well as the Qian'an Terrane, comprising granulites and retrograde amphibolites [5]. The middle–upper Proterozoic strata can be divided into three units, i.e., the Changcheng units, the Jixian units and the Qingbaikou units. The strata mainly comprise a series of unmetamorphosed or weakly metamorphosed platform-type marine-facies Mg-rich carbonates, breccias, and mudstones that represent the oldest sedimentary units on top of the crystalline basement in this area. The Paleozoic strata at Jidong mainly

include Cambrian, Ordovician and Permian units. The Cambrian and Ordovician strata comprise a set of platform-type neritic-facies sediments, which have a faulted contact with the underlying middle–upper Proterozoic strata. The Permian strata comprise a set of intra-continental basin sediments, which are mainly composed of fluvial-, lacustrine-, and swamp-facies and coal-bearing clastic rocks and continental red beds. The Jurassic mainly comprises middle Jurassic and upper Jurassic strata. The Triassic and lower Jurassic are not recorded. Only rare outcrops of Cretaceous strata are present in the eastern part. The middle Jurassic represents a set of volcanic-sedimentary rocks composed of continental red beds, intermediate volcanic rocks and volcanoclastic units. The upper Jurassic consists of intermediate to acidic sub-alkaline volcanic rocks. Folding is observed in the Archean crystalline basement. The early stage folding is characterized by tight homoclinal overturned folds with axial plane of the N–S-trending and west-dipping. The late-stage folding is characterized by open folds with axial plane of the SE or ENE trending and west-dipping [18]. Since the Triassic, the area experienced several tectonic cycles, including the Indo-China tectonic cycle, the Yanshanian tectonic cycle and the Himalaya tectonic cycle. The main fold in the area is the EW-oriented Malanyu anticlinorium, which formed during the late Jurassic. The faults in this area can be divided into three categories based on their time of formation and tectonic setting: (1) Archean faults, which represent the products of the intensive ductile compression and deformation of strata; (2) Faults that formed during the Proterozoic–Paleozoic and reactivated faults that formed during the Archean, including EW-striking compressive faults, N–S extensional faults and NE or NW-striking faults that formed under SN directed compression; (3) Faults that have formed since the Mesozoic are represented by NE–NNE compressional faults as well as NW extensional faults. The intrusions of the Jidong area are mainly presented by an arc-shaped belt. These intrusions mainly formed during the neo-Archean–Proterozoic, and the Triassic–Jurassic. The neo-Archean Shuichang granite has been dated at 3000 Ma [4]. The Yangyashan granite is dated at 2980 Ma [4]. The gray gneisses at Caozhuang and Huangbaiyu are dated to 3300 Ma [4]. The Triassic magmatic rocks mainly occur in the eastern part of the Jidong area, such as the Dushan complex (210–223 Ma) [19]. The Yanshanian intrusions are widely distributed in this area and include the Wangpingshi monzonite granite (162.3 ± 1.3 Ma) [20], the Qianfenshuiling monzonite granite (153.8 ± 2.7 Ma) [20], the Maoshan monzonite granite (162.7 ± 1.5 Ma) [20], the Tangzhangzi granite porphyry (173 ± 2 Ma) [21] and the Yuerya granite (174–175 Ma) [19], respectively.

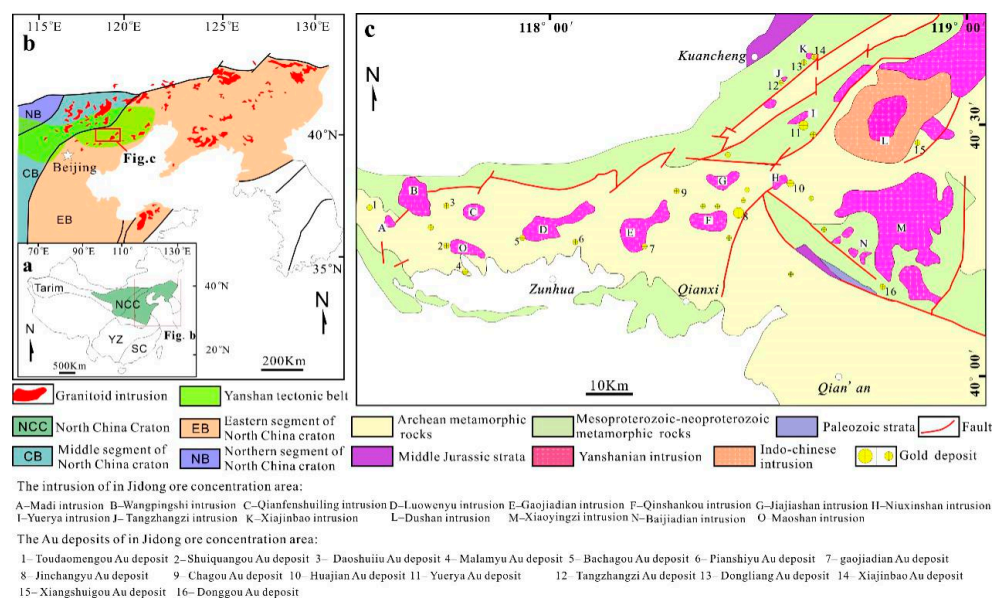


Figure 1. Simplified geological maps: (a) Major tectonic divisions of China; (b) Sketch map showing the distribution of the Triassic to Jurassic granitic intrusions in the eastern NCC; (c) Simplified geological map of the eastern Hebei Province (Modified from Mei [4] and Song et al. [5]).

3. Ore Deposit Geology

3.1. Host Rocks and Structures

The Archean Lamagou Formation of the Qianxi Group represents the oldest strata in this area (Figure 2). These strata are dominated by gray plagioclase hornblende gneiss steeply dipping to the NW at angle between 64° – 86° . The schistosity strikes at about 50° . The intermediate to basic lavas that formed on the seafloor experienced Archean regional metamorphism which produced the basement gneisses. Fractures and folds are well developed. Folds mainly occur as dome structures, with well-developed interlayered detachment zones. The fractures can be divided into 3 groups: (1) NE–NNE-striking; (2) EW-striking; and (3) SN-striking. The granite emplacement is controlled by the NE–NNE-striking faults. Its Riedel structures control the mineralization.

The Xiajinbao intrusion mainly intruded into the Archean–Jurassic strata, which have porphyritic texture. The phenocrysts mainly comprise quartz, K-feldspar and minor plagioclase. The matrix mainly comprises fine-grained K-feldspar and quartz. The K-feldspar content in the rock ranges from 35–40 vol %. The phenocrysts have a hypidiomorphic crystals. The accessory minerals include zircon and apatite. The plagioclase content of the rock is approximately 30 vol %. Plagioclase phenocrysts mainly occur as hypidiomorphic platy phases crystals, with polysynthetic and Carlsbad twinning, locally with sericite and kaolinite alteration. Quartz represents 25–30 vol % of the rock and fills the spaces between other mineral grains. Biotite comprises approximately 3 vol % of the total rock.

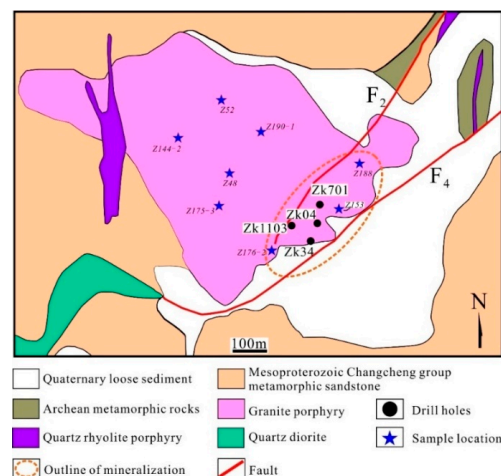


Figure 2. Geological map of the Xiajinbao gold deposit.

3.2. Ore Bodies, Ore Types and Mineralogy

The Xiajinbao gold deposit consists of 28 individual satellite ore bodies. The ore bodies are distributed in parallel veins within an area that is approximately 700 m long and 400–600 m wide; these ore bodies are mainly NE-striking and, more rarely, NNE-striking. The ore bodies dip to the NW, and they pinch and swell in places (Figure 3). The average thickness of the ore bodies is 3.02 m; they have maximum grades of 7.5 g/t, minimum grades of 1.05 g/t, and averaging 1.91 g/t of gold.

The Xiajinbao gold deposit is dominated by disseminated sulfide ores and quartz vein-type ores, with the disseminated ore commonly distributed on both sides of the quartz veins (Figure 4). The main ore minerals include native gold, electrum, pyrite, chalcopyrite, galena, sphalerite and minor tetrahedrite and molybdenite. The gangue minerals include quartz, sericite, kaolinite, carbonates, and fluorite. There are two types of gold mineralization in the area. One type occurs in the form of free-milling native gold and electrum. Another type occurs as refractory gold in pyrite, galena and sphalerite [22]. The observed ore textures include idiomorphic–hypidiomorphic, allotriomorphic, replacements, exsolutions, inclusions, and fissure-filling textures (Figure 4), respectively.

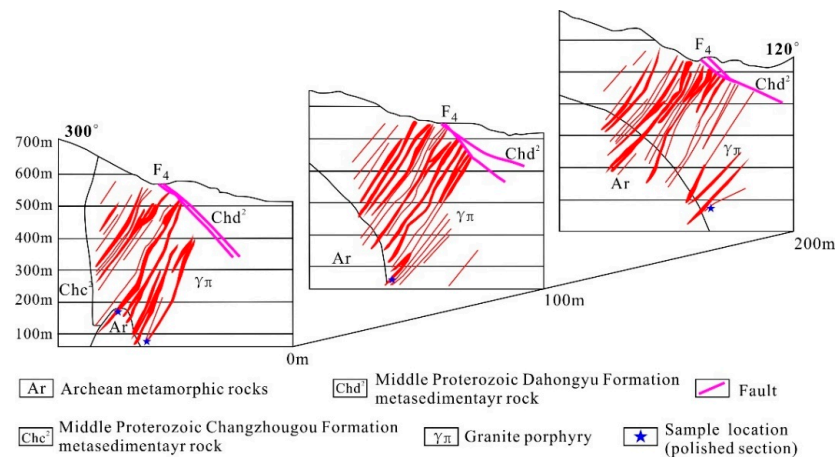


Figure 3. Joint section map of the Line 15–Line11–Line 7 ore bodies (From left to right) of the Xiajinbao gold deposit.

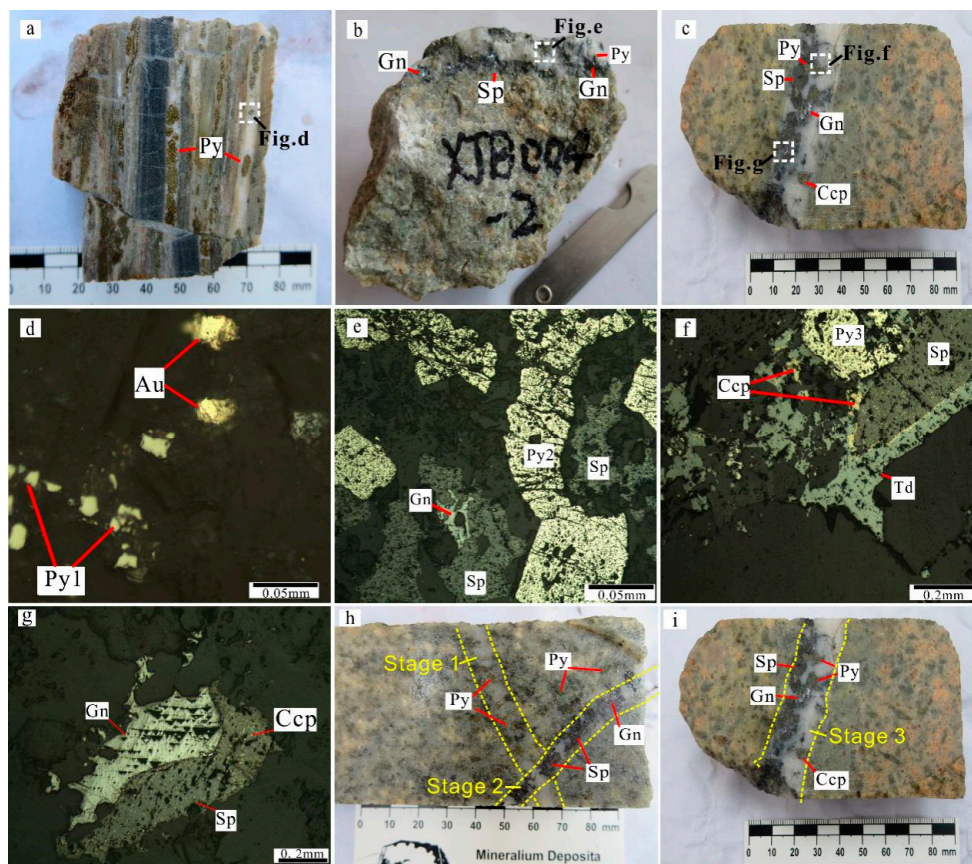


Figure 4. Mineral assemblages at the Xiajinbao Au deposit. (a) Banded auriferous pyrite–quartz–vein-type ores; (b) Galena–sphalerite–quartz–vein-bearing altered granitic porphyry; (c) Poly sulfide (pyrite, chalcopyrite, tetrahedrite, galena, sphalerite)–quartz-bearing altered granitic porphyry; (d) Native-gold–pyrite-bearing quartz vein; (e) Sphalerite replacing hypidiomorphic–allotriomorphic pyrite and replaced by galena; (f) Sphalerite replacing hypidiomorphic–allotriomorphic chalcopyrite, chalcopyrite replacing sphalerite, tetrahedrite replacing sphalerite and chalcopyrite; (g) Common intergrowth texture between galena and sphalerite; (h) Galena–sphalerite–quartz vein-cutting pyrite–quartz vein; (i) Poly sulfides (pyrite, chalcopyrite, tetrahedrite, galena, sphalerite)–quartz vein.

3.3. Alteration Assemblages

Different types of hydrothermal alteration are well developed in the Xiajinbao gold deposit and mainly include potassic alteration, sodium alteration, silicification, sericitization, kaolinization, fluoritization and carbonization. Associated ore minerals include pyrite, galena, sphalerite, chalcopyrite, tetrahedrite, and molybdenite. Silicification, sericitization, and pyritization are most intimately related to the gold mineralization. The highest grades occur within zones of silicification and sericitization.

3.4. Mineral Paragenesis

Based on previous studies regarding the overprinting relationships between ore-bearing veins and ore minerals (Figure 4h–j), the metallogenic processes can be grouped into three stages: the quartz–pyrite stage (Stage 1), the quartz–galena–sphalerite stage (Stage 2) and the quartz–polymetallic sulfide (pyrite, chalcopyrite, galena, sphalerite, and tetrahedrite) stage (Figure 5).

The quartz–pyrite stage (Stage 1): the quartz veins of Stage 1 are mainly recorded within the contact zone between the altered granitic intrusion and the wall rocks. The veins commonly have banded textures. The ore minerals include xenomorphic electrum and native gold. The gold is mainly distributed in fissures within pyrite. Pyrite mainly occurs in quartz veins.

The quartz–galena–sphalerite–pyrite stage (Stage 2): the quartz veins of the second stage also occur in the contact zone between the altered granite porphyry and the wall rocks. The ore minerals include hypidiomorphic grains of pyrite, sphalerite, galena, more rarely, electrum and native gold. Galena replacing sphalerite and sphalerite replacing pyrite are also observed. Most of the gold is distributed in fissures within pyrite, and more rarely, within sphalerite and galena. Rare gold inclusions occur in other sulfides.

The quartz–polymetallic sulfide stage (pyrite, chalcopyrite, galena, sphalerite, tetrahedrite) (stage 3): these quartz veins occur in the contact zone between the altered granite porphyry and the wall rocks as individual veins or stockworks. The ore minerals include hypidiomorphic granular pyrite, sphalerite, galena, chalcopyrite and tetrahedrite. Galena replacing sphalerite, sphalerite replacing pyrite, and tetrahedrite replacing chalcopyrite are also observed.

Stage Minerals	Stage 1	Stage 2	Stage 3
Pyrite	Abundant	Abundant	Trace
Sphalerite	Abundant	Abundant	Local
Galena	Abundant	Abundant	Local
Chalcopyrite	Abundant	Abundant	Local
Tetrahedrite	Abundant	Abundant	Trace
Quartz	Abundant	Abundant	Abundant
K-feldspar	Local	Abundant	Abundant
Biotite	Local	Abundant	Abundant
Sericite	Abundant	Abundant	Abundant
Chlorite	Local	Abundant	Local
Fluorite	Abundant	Abundant	Trace
Calcite	Abundant	Abundant	Trace

Abundant Local Trace

Figure 5. Mineral parageneses at the Xiajinbao Au deposit.

4. Sampling and Testing Methods

4.1. Sample Sites

Samples of granite porphyry were collected for major element analysis from locations shown on Figure 2. The positions of five samples for REE and trace element analyses are also shown on Figure 2.

The 8 samples for H–O isotope analyses are collected from locations detailed in Table 1. The 8 samples for S isotope analyses and five samples for Pb isotope analyses are collected from positions detailed in Table 2.

Table 1. Location and descriptions of samples for H–O isotope testing from the Xiajinbao Au deposit.

Sample No.	Location	Ore Types	Stage	Description
Z46-1	133 m, drill hole ZK401	quartz–galena–sphalerite vein	II	Vein texture; Ore minerals dominated by gold, galena, sphalerite.
Z49	97 m, drill hole ZK701	quartz–galena–sphalerite vein	II	Vein texture; Ore minerals dominated by gold, galena, sphalerite.
Z78-2	85 m, drill hole ZK501	quartz–pyrite vein	I	Vein texture; Ore minerals dominated by gold, pyrite.
Z95	64 m, drill hole ZK502	quartz–polymetallic sulfide vein	III	Vein texture; Ore minerals dominated by pyrite, chalcopyrite, galena sphalerite, tetrahedrite.
Z124	132.5 m, drill hole ZK403	quartz–pyrite vein	I	Vein texture; Ore minerals dominated by gold, pyrite.
Z148	147 m, drill hole ZK403	quartz–polymetallic sulfide vein	III	Vein texture; Ore minerals dominated by pyrite, chalcopyrite, galena sphalerite, tetrahedrite.
Z149	93 m, drill hole ZK602	quartz–pyrite vein	I	Vein texture; Ore minerals dominated by gold, pyrite.
Z158	102 m, drill hole ZK602	quartz–polymetallic sulfide vein	III	Vein texture; Ore minerals dominated by pyrite, chalcopyrite, galena sphalerite, tetrahedrite.

Table 2. Location and description of S–Pb isotope samples from the Xiajinbao Au deposit.

Sample No.	Location	Ore Types	Stage	Description
K4	open pits	quartz–pyrite vein	I	Ore minerals dominated by gold and pyrite; gangue material dominated by quartz
K5		quartz–galena–sphalerite vein	II	Ore minerals dominated by gold, galena, sphalerite; gangue material dominated by quartz
K11		quartz–galena–sphalerite vein	II	Ore minerals dominated by gold, galena, sphalerite; gangue material dominated by quartz
K13		quartz–pyrite vein	I	Ore minerals dominated by gold and pyrite; gangue material dominated by quartz
Z33		quartz–galena–sphalerite vein	II	Ore minerals dominated by gold, galena, sphalerite; gangue material dominated by quartz
K2		quartz–pyrite vein	I	Ore minerals dominated by gold and pyrite; gangue material dominated by quartz
K4		quartz–galena–sphalerite vein	II	Ore minerals dominated by gold, galena, sphalerite; gangue material dominated by quartz
K5		quartz–pyrite vein	I	Ore minerals dominated by gold and pyrite; gangue material dominated by quartz
K11		quartz–galena–sphalerite vein	II	Ore minerals dominated by gold, galena, sphalerite; gangue material dominated by quartz
K13		quartz–pyrite vein	I	Ore minerals dominated by gold and pyrite; gangue material dominated by quartz

4.2. Testing Methods

Major and trace element analyses were conducted at the ALS Laboratory Group Analytical Chemistry and Testing Services (Guangzhou, China). Major oxide concentrations were measured with an X-ray fluorescence (XRF) spectrometer. Fused glass disks with lithium borate were used, and the analytical precision is better than $\pm 0.01\%$, referring to standards GSR-2 and GSR-3. The trace element concentrations were determined by ICP-MS. Using United States Geological Survey (USGS) rock standards (basalt, Columbia River 2 [BCR-2], basalt, Hawaiian Volcanic Observatory 1 [BHVO-1], and andesite [AGV-1]), the precision and accuracy are better than $\pm 5\%$. The detailed analytical methods and procedures are described in Zhou et al. [23].

Cathodoluminescence (CL) images of the zircons were taken with a JEOL-JXA-8100 electron microprobe (JEOL Ltd., Tokyo, Japan) at GeoAnalysis Co Ltd. (Shandong Bureau Testing Center of China Metallurgical Geological Bureau, Jinan, China), operated with an acceleration voltage of 15 kV and a beam current of 2×10^{-8} A. LA-ICP-MS U–Pb zircon dating and trace element analyses were carried out at the Shandong Bureau Testing Center of China Metallurgical Geological Bureau, with a coherent 193 nm ArF excimer laser coupled to a Thermo Xseries 2 ICP-MS (Thermo Fisher Scientific, Waltham, MA, USA). Analyses were conducted with a laser diameter of 30 μm , a frequency of 8 Hz, and an energy density of $8.5 \text{ J}/\text{cm}^2$. Ablation time was 110 s, during which a blank signal was measured for 30 s, sample ablation for 55 s, and flushing 25 s, respectively. The data were corrected according to the ICP-MS Data Calsoftware provided by Liu et al. [24].

The in situ zircon Hf isotope analyses were carried out at the State Key Laboratory for Geological Processes and Mineral Resources of China University of Geosciences, Wuhan, China. The Hf isotope analyses were performed using a Neptune Plus multicollector (MC)-ICP-MS (Thermo Fisher Scientific, Waltham, MA, USA) with helium as a carrier gas, coupled to a 193 nm GeoLas laser ablation system. The laser diameter was 44 μm and the output energy density was $5.3 \text{ J}/\text{cm}^2$. Collection of the Hf and U–Pb data occurred at the same sample spots. Instrumental mass bias was corrected using standard GJ-1. The operating conditions and detailed analytical procedure are described in Hou et al. [25]. The $^{176}\text{Hf}/^{177}\text{Hf}$ weighted average of zircon standard sample GJ-1 was 0.282015 ± 28 (2 SD, $n = 10$), within error of the values reported in the literature [25,26]. The data were calculated using the ICP-MS Data Calsoftware described in Hou et al. [25] and Liu et al. [27].

The isotope samples were collected from both open pits and drill core. Pure single mineral (>95%) was selected for isotope analyses. Cu_2O was used as oxidizing agent to react with the sulfide sample to produce SO_2 , which was frozen and collected for S isotope analysis by a MAT-251 mass spectrometer. The international standard V_{CDT} (Meteorite sulfur from iron meteorites in Arizona and Dabulo canyon) was used. The accuracy was $\pm 2\%$. The Pb isotope analyses were determined using an IsoProbe-T thermal ionization mass spectrometer (TIMS, GV Instruments Ltd., Waltham, MA, USA). The Pb was separated and purified using a conventional cation-exchange technique with diluted HBr used as the eluant. The $^{208}\text{Pb}/^{206}\text{Pb}$, $^{207}\text{Pb}/^{206}\text{Pb}$, and $^{204}\text{Pb}/^{206}\text{Pb}$ ratios of the NBS981 Pb standard are 2.1681 ± 0.0008 (2σ), 0.91464 ± 0.00033 (2σ), and 0.059042 ± 0.000037 (2σ), respectively. The analyses were conducted at the Analytical Laboratory of Beijing Research Institute of Uranium Geology (BRIUG), Beijing.

The H–O isotope samples were collected from drill core. Eight mineral samples from different stages were selected for analysis. The size of the samples was around 20 mesh, with a purity of about 99.5%. The vacuum thermal explosion and zinc reduction methods were adopted to extract the hydrogen. Under vacuum conditions, and at 500–680 $^\circ\text{C}$, the BrF_5 method was used to collect pure O_2 from quartz samples, which was transferred into CO_2 . The H and O isotope analyses were conducted at the Analytical Laboratory of BRIUG using MAT-253 mass spectrometry (Thermo Electron Corporation, Waltham, MA, USA). The error range of the H isotope analyses was 0.2‰. The error range of the O isotope analyses was 2‰.

5. Results

5.1. Whole-Rock Geochemistry

The major element analyses are listed in (Table 3): (1) the rocks have very high SiO_2 content ranging from 70.420 to 72.976 wt %, low MgO of 0.413 to 0.530 wt %, low CaO of 1.360 to 1.550 wt %, and low TiO_2 (0.173–0.215 wt %) and P_2O_5 (0.065–0.078 wt %) contents, respectively; (2) The rock has $\text{Na}_2\text{O} + \text{K}_2\text{O}$ contents of 8.230–8.959 wt %, with high K_2O contents ranging from 4.560 to 5.830 wt % and $\text{Na}_2\text{O}/\text{K}_2\text{O}$ ratios ranging from 0.536 to 0.857, reflecting the high-K contents of the samples. The Rittman composite index ranges from 2.429–2.792, reflecting their calc-alkaline compositions. On the K_2O – SiO_2 diagram (Figure 6a), the sample points all fall within the high-K calc-alkaline and shoshonite fields; (3) The average alumina saturation index A/CNK value is 1.422. On the A/NK – A/CNK diagram (Figure 6b), the sample points all fall in the peraluminous field.

The trace element compositions of the Xiajinbao granite are presented in Table 4 and their spidergram patterns are shown in Figure 7a. The trace element spidergram patterns demonstrate fractional of the large-ion lithophile elements, resulting in enriched Rb, Ba and U contents and strongly depleted Nb, Ta, Sr, P, and Ti contents. These features are very similar to those of granites produced by crustal melting and subduction arc-derived granite magmas [28]. The LREE (Light rare earth elements) contents are strongly enriched, indicating that there is strong differentiation between the LREE and HREE (Heavy rare earth elements). The $(\text{Ce}/\text{Yb})_N$ values range from 7.98 to 11.29, the $(\text{La}/\text{Yb})_N$ values range from 22.17 to 32.294, and the $(\text{La}/\text{Sm})_N$ values range from 17.70 to 21.60, indicating that strong differentiation has also occurred between the light and heavy rare earth elements (Figure 7b).

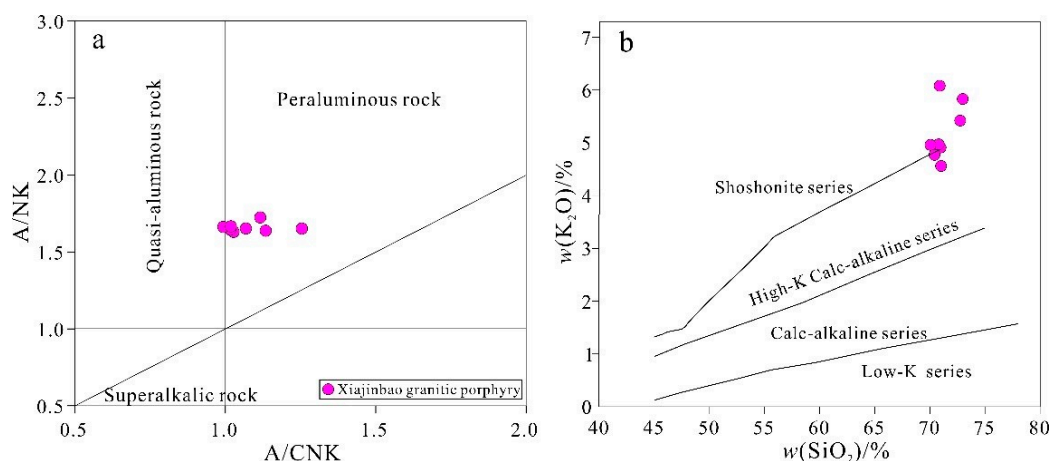


Figure 6. SiO_2 versus K_2O (a) and A/NK versus A/CNK (b) diagrams for the Xiajinbao granitic porphyry.

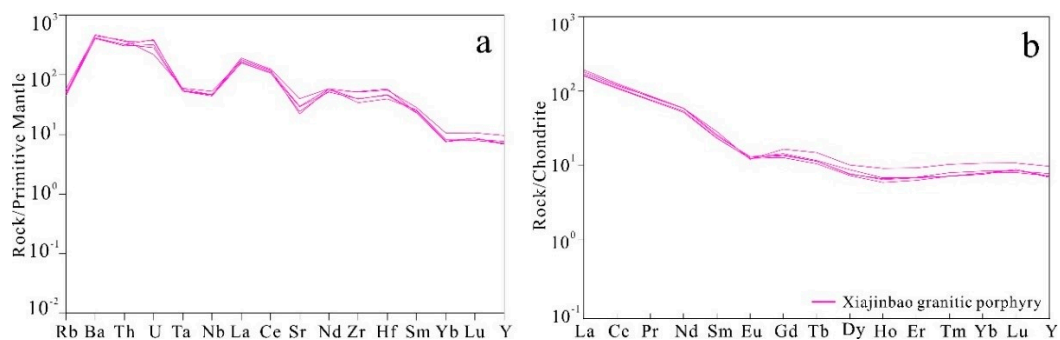


Figure 7. Primitive mantle-normalized trace element patterns (a) and Chondrite-normalized REE patterns (b) of the Xiajinbao granite.

Table 3. Chemical composition of the Xiajinbao granite (wt %).

Sample No.	Z144-2	Z153	Z176-2	Z188	Z190-1	Z175-3	Z48	Z52
SiO ₂	70.420	71.010	70.050	70.800	70.970	70.890	72.747	72.976
Al ₂ O ₃	14.330	14.080	14.300	14.310	14.110	13.920	14.607	14.792
TFe ₂ O ₃	1.940	1.870	2.160	2.210	1.990	2.450	1.269	1.342
MgO	0.493	0.413	0.454	0.482	0.521	0.480	0.530	0.498
CaO	1.540	1.550	1.510	1.480	1.460	1.478	1.396	1.360
Na ₂ O	3.830	3.910	3.730	3.330	3.630	3.420	3.538	3.126
K ₂ O	4.770	4.560	4.960	4.970	4.910	4.810	5.421	5.830
MnO	0.035	0.041	0.029	0.035	0.036	0.029	0.043	0.037
TiO ₂	0.205	0.198	0.215	0.206	0.189	0.191	0.186	0.173
P ₂ O ₅	0.078	0.074	0.076	0.075	0.078	0.075	0.069	0.065
K ₂ O + Na ₂ O	8.600	8.470	8.690	8.300	8.540	8.230	8.959	8.956
K ₂ O/K ₂ O + Na ₂ O	0.555	0.538	0.571	0.599	0.575	0.584	0.605	0.651
Na ₂ O/K ₂ O	0.803	0.857	0.752	0.670	0.739	0.711	0.653	0.536
A/NK	1.666	1.662	1.646	1.724	1.652	1.691	1.630	1.652
A/CNK	1.413	1.405	1.402	1.463	1.411	1.434	1.411	1.434
σ	2.697	2.561	2.792	2.478	2.607	2.429	2.698	2.676

A/NK = $m(\text{Al}_2\text{O}_3)/[m(\text{Na}_2\text{O}) + m(\text{K}_2\text{O})]$; A/CNK = $m(\text{Al}_2\text{O}_3)/[m(\text{CaO}) + m(\text{Na}_2\text{O}) + m(\text{K}_2\text{O})]$; $\sigma = [w(\text{K}_2\text{O}) + w(\text{Na}_2\text{O})]/[w(\text{SiO}_2) - 43]$.

Table 4. Trace element composition of the Xiajinbao granite (ppm).

Sample	Z144-2	Z153	Z176-2	Z188	Z190-1
Granitic Porphyry					
Rb	136	116	104	119	110
Ba	1083	1132	980	1001	977
Th	11	10.5	8.84	9.31	9.33
U	1.75	2.98	2.56	2.28	3.1
Ta	0.83	0.799	0.739	0.746	0.75
Nb	13	11.4	13.4	11.3	11.5
Sr	215	290	211	160	176
P	3.41	3.23	3.63	3.63	3.41
Zr	198	132	154	152	202
Hf	5.9	4.22	4.85	4.95	6.16
Ti	12.3	13.68	12.9	12.36	13.26
La	39.90	45.20	37.60	42.40	38.00
Ce	71.10	76.60	65.60	73.70	67.00
Pr	7.98	8.09	7.05	7.85	7.21
Nd	27.10	27.20	23.90	27.00	24.80
Sm	4.32	3.94	3.51	3.77	3.54
Eu	0.69	0.73	0.71	0.75	0.71
Gd	3.35	2.91	2.57	2.80	2.74
Tb	0.55	0.43	0.39	0.42	0.42
Dy	2.54	2.19	1.83	1.93	1.90
Ho	0.51	0.38	0.33	0.36	0.37
Er	1.51	1.13	1.03	1.11	1.13
Tm	0.26	0.20	0.18	0.18	0.18
Yb	1.80	1.40	1.27	1.32	1.31
Lu	0.27	0.21	0.22	0.20	0.22
Y	15.1	12	10.7	11.2	11
δEu	0.58	0.69	0.75	0.73	0.73
δCe	0.79	0.78	0.79	0.79	0.80

$\delta\text{Eu} = \text{Eu}/(\text{Sm} \cdot \text{Gd})^{0.5}$; $\delta\text{Ce} = \text{Ce}/(\text{La} \cdot \text{Pr})^{0.5}$.

5.2. Zircon Trace Elements and U–Pb Chronology

The CL images of zircons reveal idiomorphic shapes, with the development of oscillatory and rhythmical zoning (Figure 8). The widths of these zones are relatively even, indicating that the

temperature changed at relatively consistent rates during their crystallization. The zircon grains have diameters ranging from 50 to 350 μm , with length/width ratios ranging from 1:1–4:1. They are fresh and do not record evidence of hydrothermal alteration.

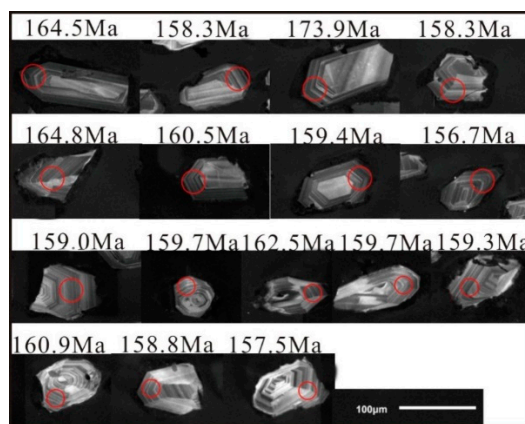


Figure 8. Representative CL images of zircon grains and $^{206}\text{Pb}/^{238}\text{U}$ ages of the Xiajinbao granite.

Zircons from different sources can have different Th and U contents. Magmatic zircons typically have high Th and U contents, and their Th/U ratios range from 0.1 to 1.0 [29,30] and commonly above 0.5 [30]. Their trace element compositions (Table 5) have Th/U ratios between 0.46 and 0.74, indicating that the zircons have primary magmatic features. In addition, the rare earth element distribution of the zircons is also similar to those of magmatic zircons (Figure 9). Therefore, the 16 zircons used for U–Pb isotopic dating are all of a magmatic origin and can be used to define the age of the granite. The results of the U–Pb chronological analyses of the Xiajinbao magmatic zircons are detailed in Table 6.

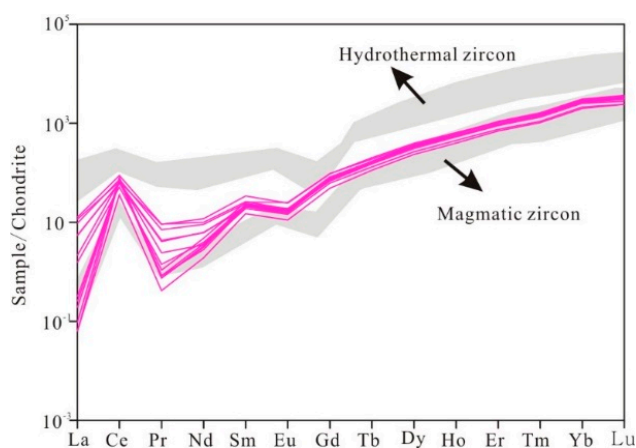


Figure 9. Chondrite-normalized REE patterns of the zircon from the Xiajinbao granite.

5.3. Hf Isotopic Compositions

The results of the zircon Hf isotopic analyses (Table 7) of the granite demonstrate that the $^{176}\text{Lu}/^{177}\text{Hf}$ ratios of both samples range from 0.000774 to 0.001561. These extremely low ratios imply that the zircons did not experience significant accumulation of radioactive Hf after crystallization. Calculations based on the ages of single zircons reveal that the $^{176}\text{Hf}/^{177}\text{Hf}$ ratios of the 16 zircons range from 0.282372 to 0.282462, with an average value of 0.282409. The zircon $\epsilon\text{Hf}(t)$ values range from -10.913 to -7.5828 . The $f_{\text{Lu}/\text{Hf}}$ values of the Xiajinbao rock body range from -0.97669 to -0.95298 , with an average value of -0.96137 . The $T_{\text{DM}2}$ values of the Xiajinbao granite range from 1496.638 to 1673.632 Ma.

Table 5. The content of trace elements for zircon from Xiajinbao granite (ppm).

Sample	Ti	Y	Nb	La	Ce	Pr	Nd	Sm	Eu	Gd	Tb	Dy	Ho	Er	Tm	Yb	Lu	Hf	Ta	Th	U
K6-01	15.68	1332	5.7	0.06	67.5	0.10	2.2	4.6	1.4	23.7	8.0	103.3	40.9	200	45.8	491	95.8	20,457	1.3	171	274
K6-02	8.2	1356	6.1	0.10	64.7	0.10	1.7	4.2	1.1	22.3	8.1	101.6	41.1	203	47.5	521	101	22,005	1.3	189	300
K6-03	13.27	956	2.9	1.2	39.7	0.40	2.7	3.3	0.85	17.6	5.7	75.2	29.3	142	32.8	359	70.2	–	0.71	94.7	171
K6-04	9.3	1508	7.1	0.02	66.5	0.09	1.9	4.5	1.3	23.0	8.2	110	45.4	229	53.6	586	113	17,118	1.6	150	279
K6-05	12.92	968	2.9	0.02	33.8	0.05	1.2	3.0	0.81	15.1	5.6	72.8	28.9	146	34.0	378	74.7	17,529	0.74	84.6	185
K6-07	17.64	1339	6.1	–	55.6	0.06	1.7	3.5	1.1	21.2	7.7	99.6	40.1	203	47.9	534	105	21,111	1.4	120	241
K6-09	18.95	1500	7.5	4.0	82.9	1.1	6.0	5.2	1.4	25.5	8.5	114	45.8	224	52.7	579	108	20,492	1.6	202	336
K6-10	7.9	1066	4.4	1.8	57.9	0.49	3.8	3.8	1.1	19.2	6.5	82.6	32.7	158	36.1	404	748	22,367	0.98	164	267
K6-11	19.36	1303	6.3	0.03	75.8	0.09	2.0	3.8	1.1	23.3	8.5	106	40.7	192	43.7	479	85.7	19,363	1.6	238	364
K6-15	11.31	880	3.4	–	51.4	0.08	1.2	2.7	0.80	16.1	5.7	71.7	27.1	132	30.5	331	60.1	13,872	0.98	152	254
Z176-16	–	1517	3.7	3.7	62.1	1.09	7.1	6.8	1.9	29.5	10.1	122	47.2	222	50.1	535	99.8	19,131	0.93	198	268
Z176-17	16.08	1440	6.1	0.7	63.5	0.29	2.1	4.1	1.3	23.1	8.2	106	43.9	217	52.2	564	111	18,141	1.4	157	277
Z176-18	–	1467	4.9	0.08	61.2	0.13	2.9	5.1	1.8	29.7	9.4	115	44.9	217	50.3	546	105	10,046	1.2	186	283
Z176-19	24.79	1340	5.5	3.1	68.8	0.85	5.4	4.8	1.3	24.2	8.2	103	40.5	199	46.2	504	96.0	24,539	1.3	191	295
Z176-29	5.4	1265	4.6	0.49	48.2	0.17	2.4	4.4	1.2	21.0	7.6	95.7	38.6	188	45.2	495	93.6	17,039	1.1	118	219
Z176-32	20.8	1324	5.3	1.7	59.6	0.52	3.7	4.3	1.2	21.9	7.6	101	40.0	197	46.4	506	96.0	21,069	1.3	159	263

“–” below detection limits.

Table 6. The results of zircon U–Pb geochronology of the Xiajinbao granite.

Sample	$w(\text{B})/10^{-6}$		Isotopic Ratio Values						t/Ma				
	Th	U	$^{207}\text{Pb}/^{206}\text{Pb}$	1 σ	$^{207}\text{Pb}/^{235}\text{U}$	1 σ	$^{206}\text{Pb}/^{238}\text{U}$	1 σ	$^{208}\text{Pb}/^{232}\text{Th}$	$^{207}\text{Pb}/^{235}\text{U}$	1 σ	$^{206}\text{Pb}/^{238}\text{U}$	1 σ
K6-01	170.8	273.9	0.0528	0.0030	0.1870	0.0105	0.0259	0.0005	0.0080	174.0	9.0	164.5	2.8
K6-02	188.7	299.5	0.0518	0.0027	0.1768	0.0097	0.0249	0.0005	0.0084	165.3	8.3	158.3	2.9
K6-03	94.7	171.0	0.0594	0.0037	0.2187	0.0131	0.0273	0.0006	0.0089	200.8	10.9	173.9	3.7
K6-04	150.0	278.8	0.0552	0.0036	0.1902	0.0136	0.0249	0.0007	0.0072	176.8	11.6	158.3	4.5
K6-05	84.6	185.3	0.0605	0.0034	0.2116	0.0115	0.0259	0.0005	0.0090	194.9	9.6	164.8	3.4
K6-07	119.8	240.6	0.0520	0.0028	0.1814	0.0101	0.0252	0.0005	0.0089	169.2	8.7	160.5	3.1
K6-09	201.8	336.2	0.0518	0.0027	0.1777	0.0092	0.0250	0.0005	0.0088	166.1	8.0	159.4	2.8
K6-10	163.8	266.8	0.0491	0.0028	0.1674	0.0095	0.0246	0.0005	0.0085	157.2	8.3	156.7	3.1
K6-11	237.7	363.6	0.0495	0.0022	0.1669	0.0070	0.0250	0.0005	0.0075	156.7	6.1	159.0	3.0
K6-15	152.1	254.1	0.0535	0.0029	0.1786	0.0087	0.0251	0.0005	0.0082	166.9	7.5	159.7	3.0
Z176-16	197.7	267.7	0.0501	0.0026	0.1725	0.0081	0.0255	0.0005	0.0077	161.5	7.0	162.5	3.1
Z176-17	157.1	277.0	0.0518	0.0023	0.1759	0.0081	0.0250	0.0004	0.0078	164.5	7.0	159.1	2.7
Z176-18	185.7	282.9	0.0476	0.0025	0.1623	0.0088	0.0250	0.0005	0.0076	152.7	7.7	159.3	3.3
Z176-19	191.0	294.6	0.0520	0.0025	0.1759	0.0085	0.0253	0.0005	0.0085	164.5	7.3	160.9	3.0
Z176-29	118.5	218.6	0.0561	0.0035	0.1830	0.0104	0.0249	0.0006	0.0081	170.7	8.9	158.8	3.8
Z176-32	143.4	243.6	0.0583	0.0033	0.1954	0.0108	0.0247	0.0006	0.0081	181.3	9.2	157.5	3.8

Table 7. The Hf isotopes of the Xiajinbao granite.

Sample	t/Ma	$^{176}\text{Hf}/^{177}\text{Hf}$	1σ	$^{176}\text{Lu}/^{177}\text{Hf}$	1σ	$^{176}\text{Yb}/^{177}\text{Hf}$	1σ	$\varepsilon_{\text{Hf}}(0)$	$\varepsilon_{\text{Hf}}(t)$	T_{DM}/Ma	T_{DMC}/Ma	$f_{\text{Lu/Hf}}$
K6-1	164.5	0.282406	0.000014	0.001509	0.000030	0.033249	0.000597	−12.950635	−9.53827	1211.893	1606.254	−0.95454
K6-2	158.3	0.282420	0.000012	0.001374	0.000020	0.030778	0.000424	−12.459401	−9.11657	1187.877	1579.874	−0.95861
K6-4	158.3	0.282408	0.000013	0.001206	0.000036	0.026823	0.000853	−12.889740	−9.27519	1199.685	1598.064	−0.96369
K6-5	164.8	0.282416	0.000012	0.001262	0.000010	0.028677	0.000229	−12.597570	−9.05277	1189.849	1583.42	−0.96198
K6-7	160.5	0.282424	0.000012	0.001187	0.000015	0.026191	0.000352	−12.299078	−8.91533	1175.589	1569.586	−0.96424
K6-9	159.4	0.282383	0.000015	0.001265	0.000043	0.028439	0.000987	−13.741773	−10.3668	1235.559	1649.706	−0.96189
K6-10	156.7	0.282421	0.000012	0.001237	0.000028	0.028503	0.000686	−12.417700	−9.03925	1181.872	1576.42	−0.96274
K6-11	159.0	0.282402	0.000012	0.001213	0.000008	0.027417	0.000189	−13.085197	−9.70445	1207.707	1613.162	−0.96346
K6-15	159.7	0.282409	0.000013	0.000774	0.000006	0.017566	0.000127	−12.828529	−9.44415	1183.666	1597.336	−0.97669
Z176-16	162.5	0.282384	0.000015	0.001440	0.000007	0.033357	0.000196	−13.727737	−10.2662	1240.788	1648.013	−0.95661
Z176-17	159.1	0.282415	0.000016	0.001345	0.000012	0.029965	0.000326	−12.613840	−9.28907	1193.124	1588.626	−0.95949
Z176-18	159.3	0.282462	0.000032	0.001561	0.000034	0.038918	0.001354	−10.948415	−7.5828	1133.043	1496.638	−0.95298
Z176-19	160.9	0.282419	0.000012	0.001440	0.000009	0.032785	0.000246	−12.478206	−9.10025	1190.719	1580.521	−0.95663
Z176-29	158.8	0.282401	0.000013	0.001276	0.000011	0.028400	0.000263	−13.117993	−9.80727	1211.03	1616.476	−0.96158

5.4. H and O Isotope Compositions

The $\delta^{18}\text{O}$ values of the fluid in equilibrium with quartz can be obtained by calculating the homogenization temperatures of the fluid inclusions of each mineralization stage based on the following equation: $\delta^{18}\text{O}_{\text{Q}} - \delta^{18}\text{O}_{\text{H}_2\text{O}} \approx 3.38 \times 10^6 / T^2 - 3.40$ [31]. The δD values of the fluid can be obtained by analyzing the fluids trapped in the inclusions of the veins (Table 8). The $\delta^{18}\text{O}$ values of the fluids of the quartz–pyrite stage (early stage) range from 7.26‰ to 8.96‰, and the δD values of the fluids range from −91.4‰ to −91‰. The $\delta^{18}\text{O}$ values of the fluids of the quartz–galena–sphalerite stage (middle stage) range from 2.34‰ to 2.74‰, while the δD values of the fluids range from −91.4‰ to −91‰. The $\delta^{18}\text{O}$ values of the fluids of the quartz–polymetallic sulfide stage (middle stage) range from −9.25‰ to −5.55‰, and the δD values of the fluids range from −96.6‰ to −83.1‰.

Table 8. H and O isotope data of quartz from the Xiajinbao gold deposit.

Sample No.	Mineral	$\delta\text{D}_{\text{V-SMOW}}$ (‰)	$\delta^{18}\text{O}_{\text{V-SMOW}}$ (‰)	$\delta^{18}\text{O}_{\text{H}_2\text{O-SMOW}}$ (‰)	Homogenization Temperature (°C)
Z46-1	Quartz	−91.4	13.6	2.34	207.0
Z49		−91	14	2.74	207.0
Z78-2		−91.4	15.8	7.26	258.9
Z95		−93.3	11.7	−5.95	151.5
Z124		−96.6	16.6	8.06	258.9
Z148		−83.1	12.1	−5.55	151.5
Z149		−88.4	17.5	8.96	258.9
Z158		−96.1	8.4	−9.25	151.5

5.5. S–Pb Isotope Compositions

The results of the S isotope analyses of the Xiajinbao gold deposit are listed in Table 9. The $\delta^{34}\text{S}$ values of the five pyrite samples range from 2.4‰ to 3.7‰, with an average value of 3.26‰. The $\delta^{34}\text{S}$ values of the five galena samples range from −0.2‰ to 0.7‰, with an average value of 0.22‰. The Pb isotope compositions of the Xiajinbao gold deposit are illustrated in Table 10. The $^{208}\text{Pb}/^{204}\text{Pb}$ ratios of the sulfides range from 35.975 to 36.204; their $^{207}\text{Pb}/^{204}\text{Pb}$ values range from 15.160 to 15.231, and their $^{206}\text{Pb}/^{204}\text{Pb}$ values range from 16.1 to 16.176.

Table 9. Sulfur isotope compositions of sulfides from the Xiajinbao gold deposit.

Sample No.	Minerals	$\delta^{34}\text{S}_{\text{V-CDT}}$ (‰)
K4	Pyrite	3.7
K5		3.4
K11		3.2
K13		3.6
Z33		2.4
K2	Galena	0.7
K4		0.1
K5		−0.2
K11		0.7
K13		−0.2

Table 10. Lead isotope compositions of sulfides from the Xiajinbao gold deposit.

Sample No.	Minerals	$^{208}\text{Pb}/^{204}\text{Pb}$	$^{207}\text{Pb}/^{204}\text{Pb}$	$^{206}\text{Pb}/^{204}\text{Pb}$	μ	ω	Th/U
K2	Galena	36.154	15.226	16.107	9.13	36.73	3.89
K4		36.204	15.231	16.176	9.12	36.53	3.88
K5		35.975	15.16	16.106	8.98	35.08	3.78
K11		36.099	15.197	16.157	9.04	35.75	3.83
K13		36.05	15.19	16.1	9.05	35.84	3.83

6. Discussion

6.1. Age of the Xiajinbao Granite and Related Au Mineralization

We present a new LA-ICP-MS zircon U–Pb age of the Xiajinbao granite of 157.8 Ma (Figure 10), which is similar to the metallogenic age (153.9 Ma, [6]) derived from zircon and apatite fission track dating and the molybdenite Re–Os model age (164.3 Ma, [7]). The gold mineralization is also spatially associated with the intrusions (Figures 2 and 3). Most of the gold deposits at Jidong are located within 0–5 km of granitic plutons [4,5]. In addition, the metallogenic ages of most of the gold deposits in the Jidong area overlap with the granitic magmatism (Table 11). For example, the SHRIMP U–Pb age of the Yuerya granite is 174–175 Ma [32]; the molybdenite Re–Os age of the Yuerya gold mineralization is 169.8 Ma [33]; the zircon LA-ICP-MS U–Pb age of the Tangzhangzi granite is 173 ± 2 Ma [21]; the molybdenite Re–Os age of the Tangzhangzi gold mineralization is 170.1 ± 1.6 Ma [34]; the SHRIMP U–Pb age of the Niuxinshan granite is 172–173 Ma [21,32]; the Ar–Ar age of the Niuxinshan (Huajian) gold mineralization is 175.8 Ma [35]; and the molybdenite Re–Os age of the Jinchangyu gold deposit is 223 ± 5 Ma. Song [5] infer that there may be a concealed middle Triassic intrusion associated with this deposit.

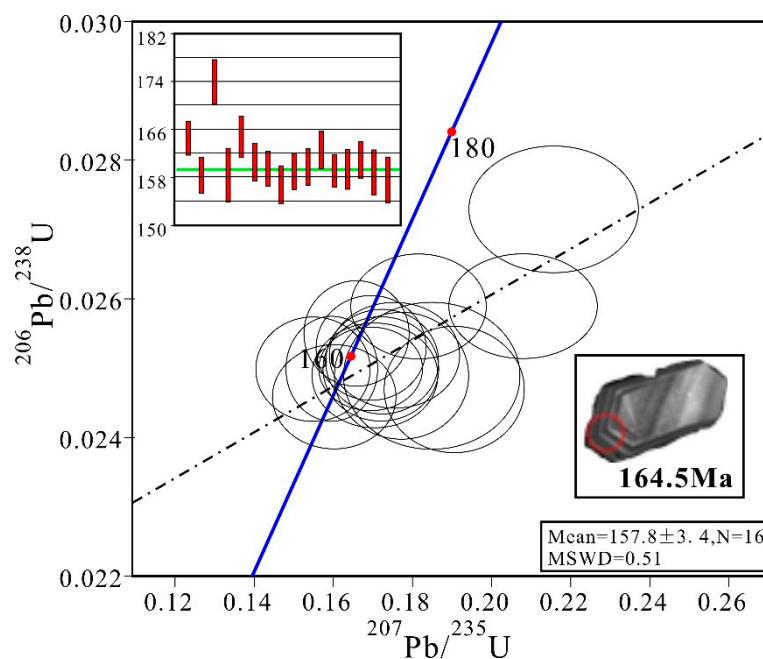


Figure 10. $^{206}\text{Pb}/^{238}\text{U}$ versus $^{207}\text{Pb}/^{235}\text{U}$ diagrams for the Xiajinbao granite.

In recent years, with the emergence of precise chronological dating methods (Table 11), the temporal evolution of the Jidong area has become relatively clear. The magmatic events in this area mainly occurred during the period of 223–153 Ma and are characterized by three main periods during the late Triassic (225–205 Ma), the early Jurassic (200–185 Ma) and the middle–late Jurassic (175–160 Ma), respectively (Figure 11). The metallogenic events in this area mainly occurred during the period of 223–155 Ma and include two main periods in the late Triassic (223–210 Ma) and middle–late Jurassic (175–155 Ma) (Figure 11), respectively. The timing of the Mesozoic magmatic activity and gold metallogenesis in the eastern Hebei ore district reveal that the gold metallogenesis correlates with the late Triassic and middle–late Jurassic magmatic events.

Table 11. The petrogenetic and ore-forming age in the Jidong gold province.

Sample Locations (Intrusion)	Host Rock	Age [Ma]	Analytical Method	Data Source
Xiajinbao	Granitic porphyry	157.0 ± 3.4	LA-MC-ICP-MS	This study
Qianfenshuiling	Monzonite granite	153.8 ± 2.7	LA-MC-ICP-MS	Yang et al. [20]
Wangpingshi	Monzonite granite	162.3 ± 1.3	LA-MC-ICP-MS	Song et al. [5]
Maoshan	Monzonite granite	162.7 ± 1.5	LA-MC-ICP-MS	
Madi	Granite	166.3	Rb–Sr	Yang et al. [20]
Qibaizi	Granite	168 ± 3	LA-ICP-MS	Song et al. [5]
	Monzonite granite	159.5 ± 0.5	LA-ICP-MS	Song et al. [5]
Xiaoyingzi	Granodiorite	164.4 ± 2.2	LA-MC-ICP-MS	Yang et al. [20]
Gaojiadian	Quartz diorite	170.5 ± 1.8	LA-MC-ICP-MS	
Niuxinshan	Granite	172–173	SHRIMP	Guo et al. [21], Luo et al. [32], Hu et al. [35]
Yuerya	Granite	174–175	SHRIMP	
Tangzhangzi	Granitic porphyry	173 ± 2	LA-MC-ICP-MS	Guo et al. [21]
Dazigou	Monzonite granite	176.5 ± 1.0	LA-ICP-MS	Luo et al. [32]
Wubaizi	Granitic porphyry	189.8 ± 0.7	LA-ICP-MS	Luo et al. [32]
Laosanjia	Granitic porphyry	196.4 ± 0.8	LA-ICP-MS	
Luowenyu	Monzonite granite	196.7 ± 7.0	LA-ICP-MS	Luo et al. [32]
Qinshankou	Monzonite granite	199 ± 2	SHRIMP	Song et al. [5], Luo et al. [32]
Liuzhuping	Monzonite granite	205.7 ± 0.8	LA-ICP-MS	Luo et al. [32]
Sanbaizi	Monzonite granite	211.1 ± 1.1	LA-ICP-MS	
Panshan	Monzonite granite	203–207	SHRIMP	Ma et al. [13]
Dushan	Granite	210 ± 4	SHRIMP	Luo et al. [19]
Dushan	Granite	223 ± 2	SHRIMP	Luo et al. [32]
Dashiyu	Granite	222 ± 1	LA-ICP-MS	Luo et al. [19]
	Monzonite granite	224 ± 2	LA-ICP-MS	
Sanjia	Granitic porphyry	222 ± 4	SHRIMP	Luo et al. [19]
Sample Locations (Deposit)	Geological Characteristics	t/Ma	Testing Method	Data Source
Xiajinbao	Altered rocks	155.73	K–Ar	Yuan et al. [6], Zou et al. [7]
Daoliushui	Ore-bearing quartz	155	Rb–Sr	Mei [4]
Maoshan	Ore-bearing quartz	174.2	K–Ar	Yang et al. [20]
Huajian	Ore-bearing quartz	175.8	Ar–Ar	Guo et al. [21], Luo et al. [32], Hu et al. [35]
Yuerya	Ore-bearing quartz	169.8	Re–Os	
Tangzhangzi	Ore-bearing quartz	170.1 ± 1.6	Re–Os	Yang et al. [20]
Shiziping	Ore-bearing quartz	179.5	Rb–Sr	Yang et al. [20]
Jinchangyu	Ore-bearing quartz	169.8/242.6	K–Ar/Re–Os	Song et al. [5]; Luo et al. [32]
Chagou	Altered rocks	166	K–Ar	Mei [4]
Xiangshuigou	Ore-bearing quartz	170.5	K–Ar	Mei [4]
Piandaogou	Ore-bearing quartz	161	Rb–Sr	Mei [4]
Shuiquangou	Ore-bearing quartz	212.5 ± 0.4	Ar–Ar	Mei [4]
Toudaomengou	Ore-bearing quartz	217.3 ± 2.0	Ar–Ar	Mei [4]

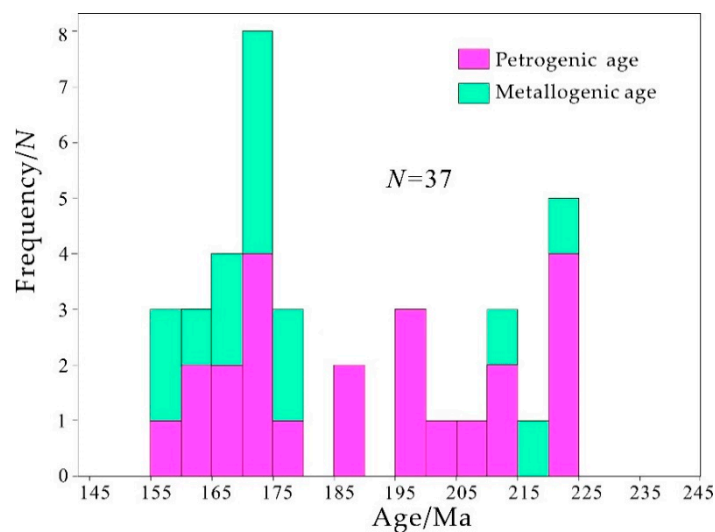


Figure 11. Histogram of petrogenic ages of granitic rocks in the Jidong gold province.

6.2. Magma Sources

The Nd/Th ratios of the Xiajinbao granite range from 2.46 to 2.90, which are similar to those of crust-derived rocks (≈ 3), but significantly different from those of mantle-derived rocks (>15) [36], thus precluding their direct derivation from the mantle. In general, mantle-derived magmas are characterized by low Lu/Yb ratios (0.14–0.15), whereas the continental crust has relatively high Lu/Yb ratios (0.16–0.18) [37]. Hence, the high Lu/Yb ratios of the samples of 0.15–0.18 also suggest that the Xiajinbao granite is likely to represent the product of crust-derived magmas. Peraluminous granites are derived from partial melting of sedimentary rocks (e.g., silty sandstone, psammite, and graywacke) [38]. The CaO/Na₂O ratio is a very important index for defining source components [28]. Peraluminous granites that form from argillaceous rocks have CaO/Na₂O values of <0.3 , and granitoids that form from psammite have CaO/Na₂O values of >0.3 [28]. The CaO/Na₂O ratios of the Xiajinbao granite range from 0.39–0.44, indicating that the magma was derived from psammitic rocks. On the Rb/Ba–Rb/Sr diagram (Figure 12a) and the CaO/(FeO^{Total} + MgO) – Al₂O₃/(FeO^{Total} + MgO) diagram (Figure 12b), the sample points also fall into the graywacke range of the clay-poor source region, indicating that this magma was derived from partial melting of crustal meta-sandstones.

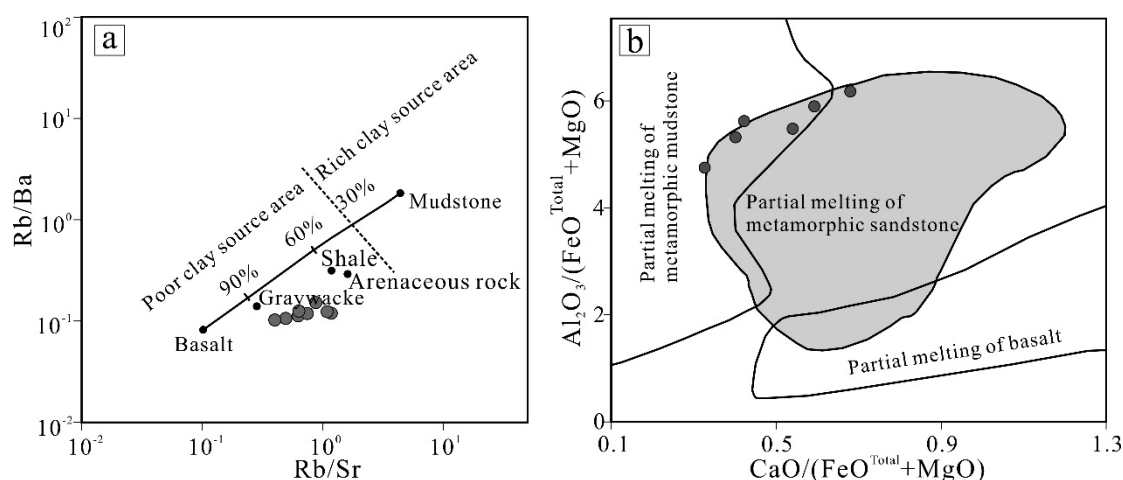


Figure 12. Rb/Sr versus Rb/Ba (a) and CaO/(FeO^{Total} + MgO) versus Al₂O₃/(FeO^{Total} + MgO) (b) diagrams for the Xiajinbao granite.

The zircon $\epsilon_{\text{Hf}}(t)$ values of the Xiajinbao granite range from -10.913 to -7.5828 . The Hf isotopic crust model ages (T_{DM2}) range from 1496.64–1673.63 Ma. The $\epsilon_{\text{Hf}}(t)$ and T_{DM2} values of both samples exhibit relatively small variation (Figure 13a). The zircon Hf isotopic compositions are relatively stable, indicating that the zircons were derived from one single source. On the $^{176}\text{Hf}/^{177}\text{Hf}$ - t diagram (Figure 13b), the zircon Hf isotopic compositions also plot in a small range above the crustal evolution line, indicating that the Xiajinbao granite was derived from partial melting of crustal material. The T_{DM2} ages obtained from the zircon Hf isotope data are close to the ages (1400–1800 Ma) of the sediments of the Changcheng Formation. Therefore, it is likely that the melts were derived from a crustal source. Comparing the zircon Hf isotopic compositions ($\epsilon_{\text{Hf}}(t)$) of the different intrusions in the Jidong area reveals that the $\epsilon_{\text{Hf}}(t)$ values of the late Triassic intrusions (e.g., the Dushan intrusion) are characterized by variable values, indicating that their magma sources represent mixtures between the mantle and the crust (Figure 13a). The $\epsilon_{\text{Hf}}(t)$ values (-13.4 to -10.8) of the middle–late Jurassic magmatic rocks (175–160 Ma) (e.g., the Baijiadian intrusion, 170.5 Ma [39]) exhibit only small variations (Figure 13a), which suggests that the Baijiadian granitic intrusion was also derived from partial melting of crustal material.

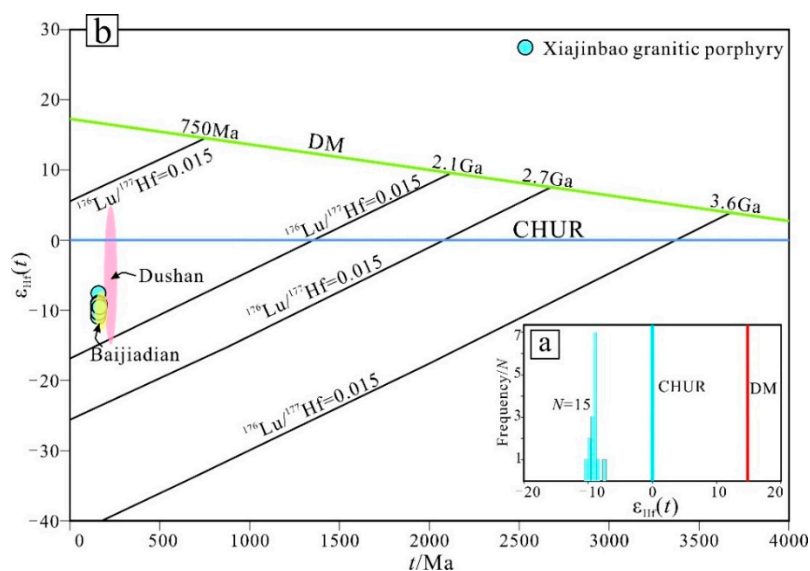


Figure 13. Histogram of $\epsilon_{\text{Hf}}(t)$ (a) and diagram of $\epsilon_{\text{Hf}}(t)$ versus U–Pb age (b) for zircons from the granitic rocks. The data from the Baijiadian and Dushan granites are from Xu et al. [39].

On the $^{207}\text{Pb}/^{204}\text{Pb}$ – $^{206}\text{Pb}/^{204}\text{Pb}$ and the $^{208}\text{Pb}/^{204}\text{Pb}$ – $^{206}\text{Pb}/^{204}\text{Pb}$ diagrams (Figure 14), the Qingshankou granite, which formed during the second period (200–185 Ma), and the Yuerya and Niuxinshan granites, which formed during the third period (175–160 Ma), all plot close to the lower crust evolution line, indicating that the magmas shared a similar source, i.e., lower crustal material. As mentioned above, the Mesozoic magmatic events can be divided into three stages. The magma composition of the late Triassic magmatic rocks suggests mixing between mantle and crustal sources. The early Jurassic magmatic rocks are derived from melting of the lower crust, for example, the Qingshankou intrusion. The middle–late Jurassic magmatic rocks are derived from melting of lower crustal material, for example, the Yuerya and Niuxinshan granites, the Baijiadian intrusion and the Xiajinbao granite, respectively.

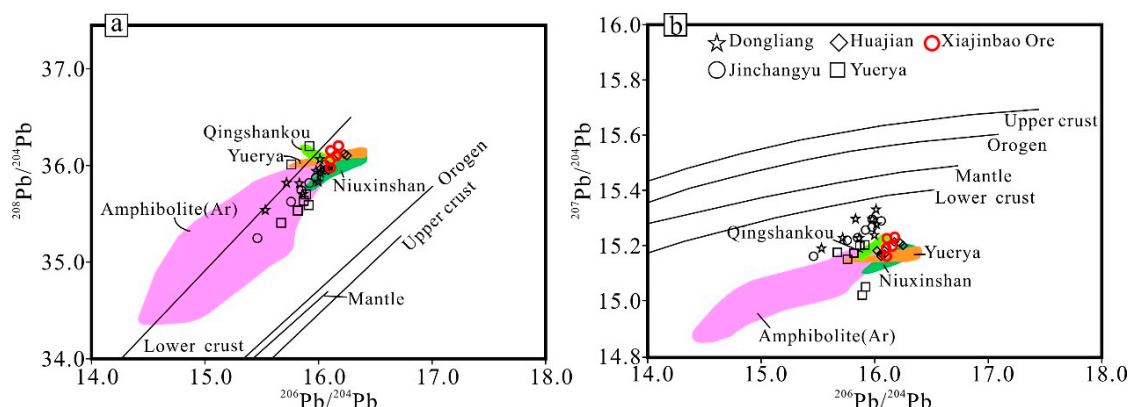


Figure 14. Diagram showing $^{208}\text{Pb}/^{204}\text{Pb}$ vs. $^{206}\text{Pb}/^{204}\text{Pb}$ (a) and $^{207}\text{Pb}/^{204}\text{Pb}$ vs. $^{206}\text{Pb}/^{204}\text{Pb}$ (b) of sulfides and granitic rocks from the Jidong area, Modified from Zartman et al. [40]. Lead isotope data of the Huajian deposit are taken from Wang [41]; Lead isotope data of the Dongliang deposit are from Xin et al. [42]; Lead isotope data of the Jinchangyu deposit are from Lin and Guo [43]; Lead isotope data of the Yuerya deposit are from Chappell [44]; Lead isotope data of the Archean plagioclase hornblende gneiss are from Lin and Guo [43], respectively.

6.3. Petrogenesis of the Xiajinbao Granite Porphyry

Granitic rocks are commonly divided into I-, S-, M- and A-type granites based on the nature of their protolith; however, M-type granitic rocks are rarely reported. Various definitions are proposed by numerous researchers [44–47]. Based on Na_2O – K_2O diagrams, previous studies concluded that the Xiajinbao granite porphyry represents an A-type granite [48]. However, A-type granites usually have very characteristic geochemical features (e.g., high FeO^T/MgO ratios and high field strength element (HFSE) contents) [47]. The Zr values of the major minerals are low, suggesting that their crystallization had little impact on the Zr content of the evolving magma [49]. Due to the behavior of Zr relatively immobile during hydrothermal alteration, the variations in its contents are commonly used as an indicator for magmatic differentiation. On the Zr– FeO^T/MgO diagram (Figure 15a), the FeO^T/MgO ratios and Zr values show a positive correlation, consistent with the evolved composition of the granites. A typical granitic melt has very little variation of Y/Ho values, which are typically close to the chondritic Y/Ho ratio (27.7 ± 1.9 [50]). However, interactions between the rock and fluids could result in a wider range of variation of Y/Ho values [51]. The Y/Ho ratios of the Xiajinbao granitic porphyry range from 29.61 to 32.42, which are higher than that of chondrite (27.7 ± 1.9 [50]), indicating that the magma experienced magma–fluid interaction during its evolution. On the Y/Ho– FeO^T/MgO diagram (Figure 15b), the FeO^T/MgO and Y/Ho values show a positive correlation, indicating that the high FeO^T/MgO ratios of the Xiajinbao granite could have resulted from interactions between the magma and fluids. The division of I-type and S-type granites is based on the magma source [45]. As mentioned above, the Xiajinbao granite represents a peraluminous rock ($\text{A}/\text{CNK} = 0.89\text{--}1.13$, averaging 1.422), which was derived from partial melting of the Changcheng meta-graywacke and thus can be classified as S-type granite. However, the Xiajinbao granite does not contain Al-rich minerals, such as cordierite, garnet, and primary muscovite. During magmatic differentiation, the P_2O_5 contents of the Xiajinbao granite tend to decrease (Figure 15c), in contrast to S-type granites [52]. Low P_2O_5 content is a significant criterion for distinguishing I-type from S-type granites [28]. On the P_2O_5 –Rb diagram (Figure 15d), the Xiajinbao granite falls into the range of I-type granites.

6.4. The Source of Ore-Forming Materials

The $\delta^{18}\text{O}_{\text{H}_2\text{O}}$ values of the quartz that formed during the early mineralization period range from 7.26–8.96‰, which are consistent with O isotope compositions (5.5–9.5‰) of magmatic water defined by Sheppard [53]. The $\delta^{18}\text{O}_{\text{H}_2\text{O}}$ values of the quartz during the quartz–galena–sphalerite

stage (Stage 2) and the quartz–polymetallic sulfide stage (Stage 3) from 2.34‰ to 2.74‰ and from 9.25‰ to −5.55‰, respectively, which are consistent with the O isotope composition of meteoric water, indicating an increasing influence of meteoric waters during the mineralization. On the δD – $\delta^{18}O_{H_2O}$ plot (Figure 16), the samples from the Xiajinbao, Jinchangyu, Yuerya, Tangzhangzi, Dongliang and Huajian gold deposits all fall into the field of magmatic water or they range between magmatic and meteoric waters during their evolution.

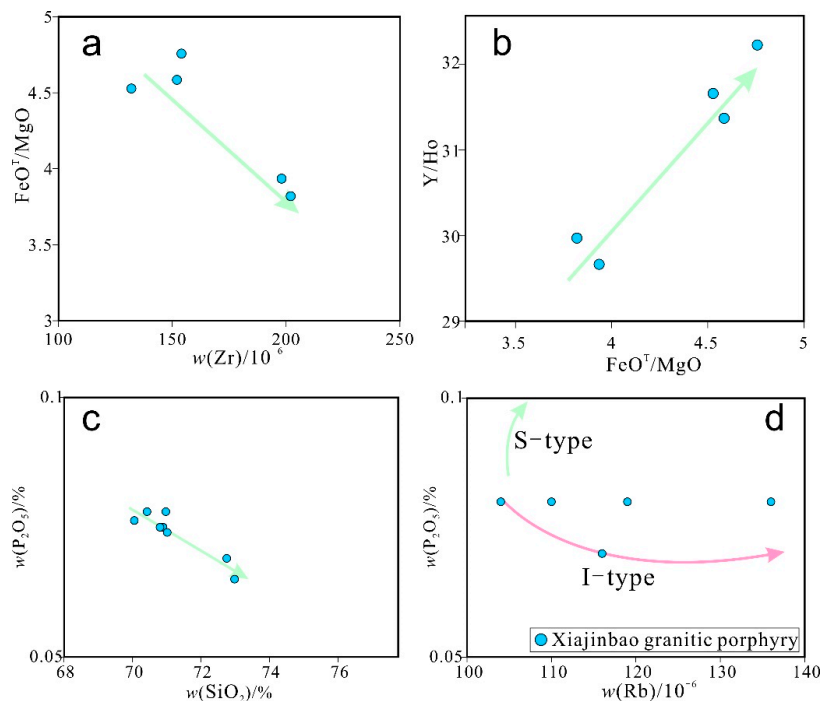


Figure 15. FeO^T/MgO vs. SiO_2 (a), Y/Ho vs. FeO^T/MgO (b), P_2O_5 vs. SiO_2 (c), and Rb vs. P_2O_5 (d) diagrams for the Xiajinbao granite porphyry.

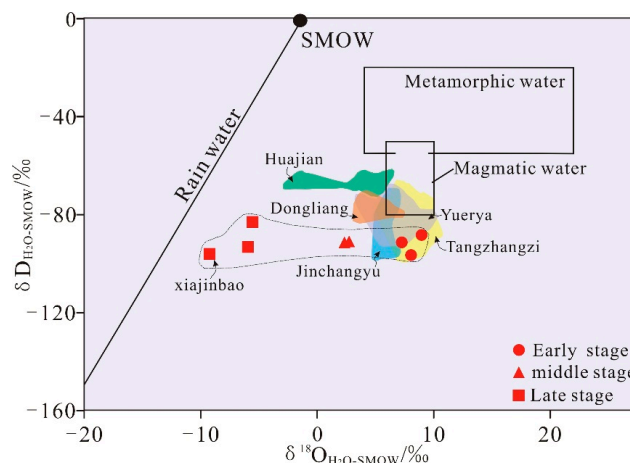


Figure 16. Oxygen and hydrogen isotope compositions of quartz and ore-forming fluids from the Jidong gold deposits. Oxygen and hydrogen isotope data of the Huajian deposit are from Shi [41] and Wang [54]; Oxygen and hydrogen isotope data of the Dongliang deposit are from Xin et al. [42]; Oxygen and hydrogen isotope data of the Jinchangyu deposit are from Zhang et al. [55]; Oxygen and hydrogen isotope data of the Yuerya deposit are from Jie [56]; Oxygen and hydrogen isotope data of the Tangzhangzi deposit are from He [57].

Ohmoto [58] suggests that the $\delta^{34}\text{S}$ values of hydrothermal sulfides are functions of the $\delta^{34}\text{S}$ values of the hydrothermal fluids, oxygen fugacity ($f\text{O}_2$), temperature, pH, and ionic potential, i.e., $\delta^{34}\text{S}_{\text{mineral}} = f(\delta^{34}\text{S}_{\Sigma\text{S}}, f\text{O}_2, T, \text{pH}, I)$. The $\delta^{34}\text{S}$ values of the hydrothermal minerals depends not only on the $\delta^{34}\text{S}$ values of the source region, but also on the physical and chemical conditions during the transport and precipitation of sulfur in the hydrothermal fluid. Ohmoto [59] suggests that the $\delta^{34}\text{S}$ values of the hydrothermal fluid should be similar to those of the sulfides, namely, $\delta^{34}\text{S}_{\Sigma\text{S}} \approx \delta^{34}\text{S}_{\text{sulfide}}$, in a hydrothermal system with a relatively simple mineral assemblage in the absence of sulfates. No sulfate minerals were found at the Xiajinbao gold deposit, and its mineral composition is relatively simple, mainly comprising quartz, pyrite, galena, sphalerite and chalcopyrite. Therefore, its sulfide composition should represent the total sulfur composition of the hydrothermal system. The $\delta^{34}\text{S}$ values of the Xiajinbao deposit (-0.2 to 3.7‰) are similar to those of a magmatic-hydrothermal system ($0 \pm 5\text{‰}$ [58]) and slightly lower than those of the crust (mean $+7\text{‰}$ [60]), indicating that the sulfur of the Xiajinbao deposit was derived from magmatic-hydrothermal sources. Additionally, the sulfide isotope compositions of other gold deposits such as the Jinchangyu, Yuerya, Tangzhangzi, Dongliang and Huajian gold deposits all fall into the range of $0 \pm 5\text{‰}$, indicating that Mesozoic magmatism also provided a source of sulfur for the formation of these gold deposits. On the S isotope distribution diagram (Figure 17), the S isotope compositions of the above-mentioned gold deposits plot close to the S isotopic composition of the Archean plagioclase hornblende gneisses, indicating that these gneisses also provided a source of sulfur for the gold deposits at Jidong.

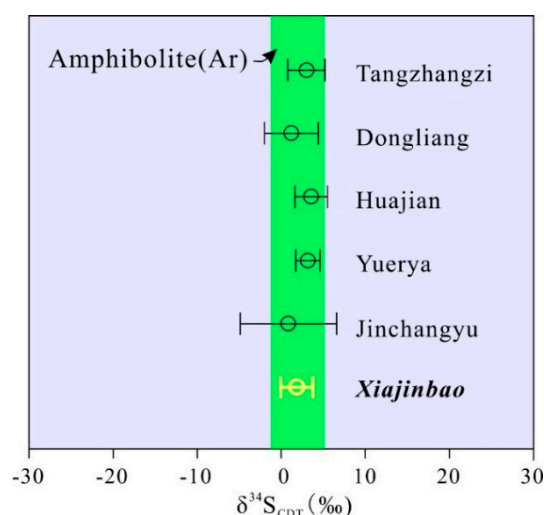


Figure 17. Sulfur isotope compositions of quartz and ore-forming fluids from the Jidong area. Sulfur isotope data of the Huajian deposit are from Shi [41] and Wang [54]; Sulfur isotope data of the Dongliang deposit are from Xin et al. [42]; Sulfur isotope data of the Jinchangyu deposit are from Zhang et al. [55]; Sulfur isotope data of the Yuerya deposit are from Jie [56]; Sulfur isotope data of the Tangzhangzi deposit are from He [57]; Sulfur isotope data of the Archean plagioclase hornblende gneiss stratum are from Lin and Guo [43].

On both the $^{207}\text{Pb}/^{204}\text{Pb}$ – $^{206}\text{Pb}/^{204}\text{Pb}$ diagram and the $^{208}\text{Pb}/^{204}\text{Pb}$ – $^{206}\text{Pb}/^{204}\text{Pb}$ diagram (Figure 14), the data (from the Xiajinbao, Jinchangyu, Yuerya, Tangzhangzi, Dongliang and Huajian gold deposits) form a clear linear relationship. In a 2-end-member system, all Pb isotope data fall on a line between two end members. In a 3-end-member system, all data plot in the triangular zone defined by three end members [61]. Therefore, Figure 14 showing linear relationship suggests that the source of Pb in these deposits likely originated two end members. The Pb isotopic compositions of the Xiajinbao, Jinchangyu, Yuerya, Tangzhangzi, Dongliang, and Huajian gold deposits in this area are not only related to the granitic magma, both temporally and spatially, but are also close to those of the Archean plagioclase

hornblende gneiss (Figure 14). Overall, the S and Pb compositions of the Jidong gold deposits are all derived from the Mesozoic granitic magma and the Archean plagioclase hornblende gneisses.

6.5. Origin of the Granite Porphyry and Related Xiajinbao Au Mineralization

The magmatic age (157 Ma) corresponds to the simultaneous movement of several plates (i.e., the Siberia plate, the Mongolia–Northern China plate and the Paleo–Pacific plate), which caused intra-continental collision and orogenic movement along the northern margin of the North China plate, resulting in crustal compression and thickening [62–70]. The simultaneous subduction of several plates (i.e., the Siberia plate, the Mongolia–Northern China plate and the Paleo–Pacific plate, [62–70]) caused the continuous thickening and partial melting of the Changcheng meta-graywacke in this area, resulting in the formation of Au-rich granitic magmas. The magmatic-hydrothermal brines associated with I-type magmas can transport the metals, including gold, and sulfur required for ore formation [71]. When primitive magmatic fluids migrated along structures, the metals from the Archean plagioclase hornblende gneiss were leached, thus forming the metallogenic fluids. Under medium to low temperatures, gold is usually transported as Au-S(H) complexes such as $\text{Au}(\text{HS})_2^-$ [72,73]. As a result of a decreasing temperature or a sudden pressure release, the gold-bearing complexes were destabilized, resulting in the precipitation of gold [8]. The remaining S^{2-} and Fe^{2+} precipitated as pyrite, forming the early stage auriferous pyrite–quartz veins. As the metallogenic process continued, there was an influx of meteoric water. The mixing process of the fluids was accompanied by oxidation and the loss of H_2S , which were the main reasons for the destabilization of the gold-bearing sulfide complexes in the middle–late-stage quartz veins [74]. The remaining S^{2-} combined with metals such as Cu^{2+} , Fe^{2+} , Pb^{2+} and Zn^{2+} to precipitated as chalcopyrite, galena and sphalerite.

Many scholars believe that the Xiajinbao gold deposit belongs to a porphyry-type gold deposit because (1) its metal contents are mainly derived from the Xiajinbao granite intrusion [8,9,48]; (2) its metallogenic fluids have high salinity, similar to porphyry deposits [8]; (3) the Sb and Bi contents in the auriferous galena are similar to those of some porphyry-type deposits in the Western Henan Province [75]; and (4) the auriferous pyrite has high contents of Cu, Pb, Zn, Sb, Ag, and Au, which is similar to pyrite from mesothermal gold deposits and porphyry deposits [9]. The Xiajinbao gold deposit also shows many features similar to those of intrusion-related gold deposits, while porphyry Cu–Au deposits are generally associated with dominantly oxidized, magnetite-series and less fractionated calc-alkaline to alkaline magmatic suites that have affinities with magmatic and/or island arcs (e.g., References [76,77]), intrusion-related Au deposits are associated with more reduced I-type, calc-alkaline intrusions [78]. Compared with the more oxidized and less fractionated granitoids associated with porphyry systems [79,80], the Xiajinbao Au deposit is associated with highly fractionated (high Rb/Sr ratios of 0.40 to 0.74, Avg. 0.58) I-type granitoids; additionally, the Xiajinbao granitic magma also exhibits low oxidation states [81]. In contrast to porphyry Cu–Au systems, which are generated in subduction-related settings, the Xiajinbao Au deposit formed in a complex tectonic setting during the simultaneous movement of several plates (i.e., the Siberia plate, the Mongolia–Northern China plate and the Paleo–Pacific plate), similar to the intrusion-related Au deposits of the Yilgarn Craton that are located in a tectonic setting inboard of a convergent plate margin [82–84]. (3) In general, ore-zone geometries mainly depend on the overall form of the host stock or dike complex [85,86]. However, the gold ore bodies in this area are mainly distributed as parallel veins that are NW-dipping, NE-striking, and structurally controlled by NE-striking faults (Figures 2 and 3), which is inconsistent with typical porphyry-type deposits [86]. By contrast, these ore bodies show features of intrusion-related gold deposits, such as the Tintina gold belt in Yukon, Canada [78,87]. The spatial pattern of the wall rock alteration of the Xiajinbao deposit is controlled by F_2 faults, showing an NNE-striking orientation (Figure 2). In addition, the spatial distribution of alteration at Xiajinbao does not show alteration pattern of porphyry-type deposits. The alteration types in this area include K-alteration and Na-alteration pre-dating the metallogenic stage and silicification, sericitization, carbonization, and kaolinization during the main metallogenic stage, which are similar to those observed in other intrusion-related

gold deposits. Furthermore, gold precipitation is always closely related to sericitization [78]. (5) The hydrothermal fluids are characterized by moderate temperatures, moderate to low salinities, low alkali contents, low fO_2 and high CO_2 contents [48]. These characteristics are all similar to those of the metallogenic fluids from intrusion-related gold deposits and different from those from porphyry-type deposits [78].

6.6. Evolution of the Mesozoic Gold Mineralization in the Jidong Area

During the Archean, the crust was relatively thin and active, accompanied by intensive magmatic activity. Basic to ultra-basic volcanic rocks were formed. As a result of regional metamorphism, the mafic plagioclase hornblendite gneisses with high Au background values formed [4,9,88].

After the late Paleozoic, the area was affected by several plate subduction collision events (i.e., the Siberia plate, the Mongolia–Northern China plate and the Paleo–Pacific plate, [62–70]), including the closure of the Paleo–Pacific Ocean, the closing of the Mongolia–Okhotsk Ocean, and the subduction of the Paleo–Pacific Ocean [62–64]. After the closure of the Mongolian plate and the Northern China plate along the Sauron suture during the late Permian [24,89], the eastern Hebei area (on the northeastern edge of the Yanshan tectonic belt) was subject to post-collisional extension [90,91]. Meanwhile, asthenospheric mantle upwelling transformed the lower crust. Mantle-derived magma underplated the bottom of the lower crust, triggering intensive mantle–crust interaction and inducing partial melting of the ancient lower crust [91]. The mantle–crust-derived magma intruded along fractures, marking the first episode of magmatic activity at ca. 225–205 Ma and the first episode of gold mineralization at about ca. 223–210 Ma (Figure 18a) during the Mesozoic. When the magma intruded into metamorphic rock strata, the differentiated magmatic water transformed the primitive ore source strata (Archean plagioclase hornblende gneiss) and leached the gold from the strata. Hydrothermal fluids associated with magmatism formed the Jinchangyu gold deposit [88].

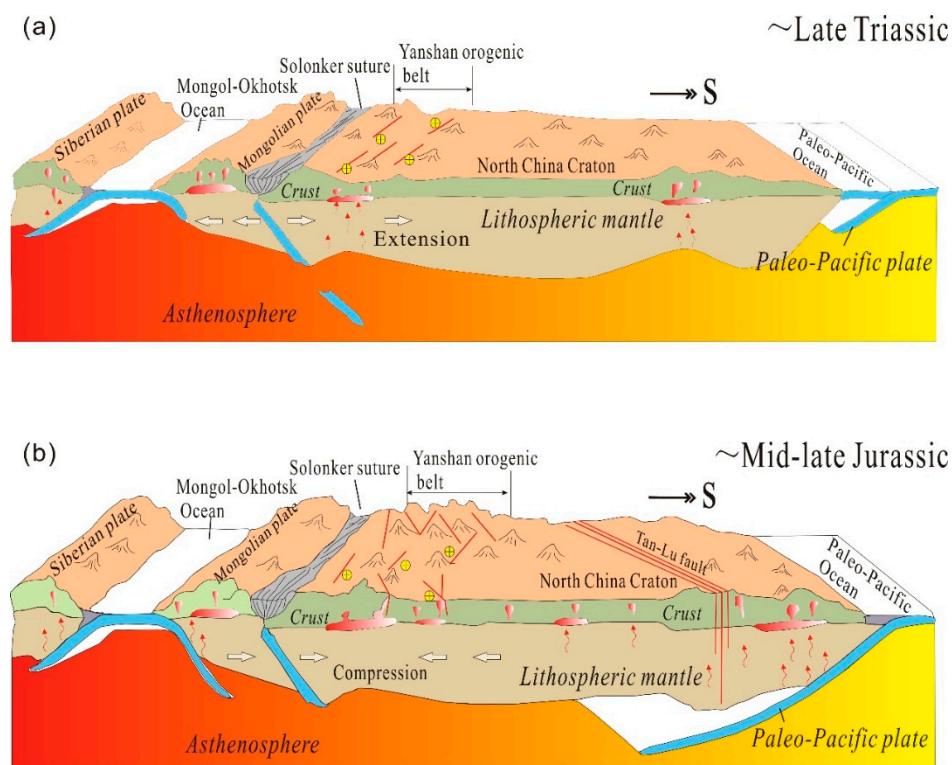


Figure 18. A simplified mineralization model of the Jidong gold province, modified from Ma [92]. (a) gold mineralization model and tectonic setting of Late Triassic in Jidong area; (b) gold mineralization model and tectonic setting of Mid–Late Jurassic in Jidong area.

During the early Jurassic, the Northern China–Mongolia plate collided with the Siberia plate, and the Mongolia–Okhotsk Ocean gradually closed from west to east [65–67]. This resulted in the NE compression and the formation of the Yanshanian orogenic belt, leading to the thickening and melting of the crust and resulting in the early Jurassic magmatic activity in this area, such as the Qingshankou granite. During the middle–late Jurassic, the Paleo–Pacific plate subducted beneath the Northern China plate along a NW trench [67–70]. The simultaneous subduction of several plates caused the continuous thickening of the crust along the northern margin of the Northern China plate during the middle and late Jurassic. As a result, the magma derived from partial melting of the crust intruded along fractures, resulting in the 175–160 Ma magmatic activity of this area (e.g., the Xiajinbao granite porphyry, Baijiadian granite, Yuerya granite, and Niuxinshan granite) as well as the second phase of gold metallogenesis (ca. 175–155 Ma) (Figure 18b). Different magmatic emplacement mechanisms resulted in gold deposits of different types: (1) when the magma experienced a cryptoexplosion during its intrusion, it would result in the formation of a cryptoexplosion-type gold (molybdenum) deposit–vein-type gold deposit hosted by phreatic breccias or by granite porphyry breccias, such as the Tangzhangzi gold deposit [34]; (2) when the magma was emplaced within a clastic sediment (meta-sandstone), it would result in the formation of a hydrothermal gold deposit, intrusion-related gold deposit and/or porphyry-type gold deposit, such as the Huajian gold deposit [54], the Dongliang gold deposit [92], the Yuerya gold deposit (part of the ore bodies) [56], and the Xiajinbao gold deposit, respectively; (3) when the magma was emplaced into a chemically reactive stratum (e.g., limestone), it would result in the formation of skarn-type gold deposits, such as the Yuerya gold skarn [56].

7. Conclusions

- (1) The Xiajinbao granite porphyry have relatively high SiO₂, K₂O contents; but low MgO and CaO contents; high-K calc-alkaline to shoshonitic characteristics. The rock is enriched in LREE and large ion lithophile elements (LILE) such as Rb, Ba and U, and it is strongly depleted in HREE and in HFSE and Sr, P. The petrographic features, major and trace elements, and zircon Hf isotopic model ages suggest that the Xijinbao granite is derived from partial melting of the Changcheng sediments.
- (2) The zircon LA-ICP-MS age of the Xiajinbao granite is 157.8 ± 3.4 Ma, which is close to the gold metallogenic age (153.9–163.4 Ma), indicating that both are related to the same tectonic setting.
- (3) H–O isotope of the auriferous quartz vein show that the early metallogenic fluids are derived from magmatic waters, while increasingly more meteoric water mixed with this fluid. S–Pb isotope results show that the metals were derived from both the magma and plagioclase hornblende gneisses.
- (4) The gold mineralization of the Xiajinbao deposit is closely associated with the high-K calc-alkaline to shoshonitic granite magma emplaced during the Yanshannian collision. The Xiajinbao deposit is an intrusion-related gold deposit.
- (5) The magmatic events mainly occurred during the period between 223–153 Ma, characterized by three main periods during the late Triassic (225–205 Ma), the early Jurassic (200–185 Ma) and the middle–late Jurassic (175–160 Ma), respectively. The metallogenic events mainly occurred during the period between 223 Ma and 155 Ma, including two main periods during the late Triassic (223–210 Ma) and during the middle–late Jurassic (175–155 Ma).

Author Contributions: C.W., Y.S., and Q.L. conceived and designed the experiments; C.W., J.Z., and Z.L. performed the experiments; all authors wrote the paper.

Funding: This research was funded by [the Innovation-driven Plan of Central South University] grant number [1053320180985] and [the Open Topic of Hunan Key Laboratory of Land Resources Evaluation and Utilization] grant number [SYS-ZX-201804].

Acknowledgments: This work was supported by the Innovation-driven Plan of Central South University (Project 1053320180985) and the Open Topic of Hunan Key Laboratory of Land Resources Evaluation and Utilization (Project SYS-ZX-201804).

Conflicts of Interest: The authors declare no conflict of interest.

References

- Hart, C.J.R.; Goldfarb, R.J.; Qiu, Y.; Snee, L.; Miller, L.D.; Miller, M.L. Gold deposits of the northern margin of the North China Craton: Multiple late Paleozoic–Mesozoic mineralizing events. *Miner. Depos.* **2002**, *37*, 326–351. [[CrossRef](#)]
- Wang, W.; Liu, S.; Santosh, M.; Deng, Z.; Guo, B.; Zhao, Y.; Zhang, S.; Yang, P.; Bai, X.; Guo, R. Late Paleoproterozoic geodynamics of the North China Craton: Geochemical and zircon U–Pb–Hf records from a volcanic suite in the Yanliao rift. *Gondwana Res.* **2015**, *27*, 300–325. [[CrossRef](#)]
- Cook, N.J.; Ciobanu, C.L.; Mao, J. Textural control on gold distribution in As-free pyrite from the Dongping, Huangtuliang and Hougou gold deposits, North China Craton (Hebei Province, China). *Chem. Geol.* **2009**, *264*, 101–121. [[CrossRef](#)]
- Mei, Y.X. The Metallogenic Characteristic and Evolution of Gold Deposits in Jidong Region, Hebei Province, China. Ph.D. Thesis, Chinese Academy of Geological Sciences, Beijing, China, 1997. (In Chinese)
- Song, Y.; Jiang, S.H.; Bagas, L.; Li, C.; Hu, J.Z.; Zhang, Q.; Zhou, W.; Ding, H.Y. The geology and geochemistry of Jinchangyu gold deposit, north China Craton: Implications for metallogenesis and geodynamic setting. *Ore Geol. Rev.* **2016**, *73*, 313–329. [[CrossRef](#)]
- Yuan, W.M.; Wang, S.C.; Wang, L.F. Fission track study on the metallogenetic age of Xiayingfang gold deposit in eastern, Hebei. *Nuclear Tech.* **1999**, *22*, 411–413. (In Chinese)
- Zou, T.; Wang, Y.W.; Wang, J.B.; Zhang, H.Q.; Zhao, L.T.; Xie, H.J.; Shi, Y.; Liu, Y.Z.; Liu, G.Q. Geochronology of the Xiayingfang Au Deposit in Eastern Hebei Province. *Geol. Explor.* **2016**, *52*, 84–97. (In Chinese)
- Luan, W.L.; Yu, Y.X. Geochemistry of fluid inclusion of Xiayingfang gold deposit in Pingquan of Hebei province and ore-searching significance. *J. Precious Met. Geol.* **1995**, *4*, 161–167. (In Chinese)
- Yang, T.D. The study of complex mineralization and metallogenic series of Xiayingfang gold deposit, Hebei province. *Earth Sci.* **1989**, *12*, 405–413. (In Chinese)
- Shao, J.L.; Mei, J.M. Study on pyrite in a volcanic gold deposit in Pingquan, Hebei Province. *Gold* **1984**, *5*, 3–8. (In Chinese)
- Jia, S.; Wang, E.; Fu, J. Geological differences and mineralization unity of the key gold ore concentrated regions in eastern Hebei and Western Liaoning provinces. *Acta Geol. Sin.* **2011**, *85*, 1493–1506. (In Chinese)
- Liu, D.Y.; Nutman, A.P.; Compston, W.; Wu, J.S.; Shen, Q.H. Remnants of ≥ 3800 Ma crust in the Chinese part of the Sino-Korean craton. *Geology* **1992**, *20*, 339–342. [[CrossRef](#)]
- Ma, Y.S.; Zeng, Q.L.; Song, B.; Du, J.J.; Yang, F.Q.; Zhao, Y. SHRIMP U–Pb dating of zircon from Panshan granitoid pluton in Yanshan orogenic belt and its tectonic implications. *Acta Petrol. Sin.* **2007**, *23*, 547–556. (In Chinese)
- Niu, S.Y.; Li, F.Y.; Chen, H.S.; Sun, A.Q.; Wang, B.D.; Wang, J.Z.; Ma, B.J. The exploration and prognosis in the depth and the periphery of the Jinchangyu gold deposit in eastern Hebei. *Chin. Geol.* **2012**, *39*, 999–1006. (In Chinese)
- Zhang, G.R.; Xu, J.H.; Wei, H.; Song, G.C.; Zhang, Y.B.; Zhao, J.K.; He, B.; Chen, D.L. Structure, alteration, and fluid inclusion study on deep and surrounding area of the Dongping gold deposit, northern Hebei, China. *Acta Petrol. Sin.* **2012**, *28*, 637–651. (In Chinese)
- Huang, X.; Ziwei, B.; DePaolo, D.J. Sm–Nd isotope study of early Archean rocks, Qian’an, Hebei Province, China. *Geochim. Cosmochim. Acta* **1986**, *50*, 625–631. [[CrossRef](#)]
- Jahn, B.M.; Auvray, B.; Cornichet, J.; Bai, Y.L.; Shen, Q.H.; Liu, D.Y. 3.5 Ga old amphibolites from eastern Hebei Province, China: Field occurrence, petrography, Sm–Nd isochron age and REE geochemistry. *Precambrian Res.* **1986**, *34*, 311–346. [[CrossRef](#)]
- Sun, D.Z. *The Early Precambrian Geology of the Eastern Hebei*; Tianjin Science and Technology Press: Tianjin, China, 1984; pp. 1–273. (In Chinese)
- Luo, Z.K.; Miao, L.C.; Guan, F.; Qiu, Y.S.; Qiu, Y.M.; McNaughton, N.J.; Groves, D.I. SHRIMP U–Pb zircon dating of the Dushan granitic batholith and related granite-porphyry dyke, eastern Hebei Province, China, and their geological significance. *Geochimica* **2003**, *32*, 173–180. (In Chinese)

20. Yang, F.L.; Niu, B.G.; Ren, J.S.; Li, S. Zircon U–Pb ages and geochemical characteristics of the Mesozoic intrusive bodies along the core of the Malanyu anticline and their tectonic significances. *Acta Geosci. Sin.* **2015**, *36*, 455–465. (In Chinese)
21. Guo, S.F.; Tang, Z.L.; Luo, Z.H.; Zhao, W.H. Zircon SHRIMP U–Pb dating and geological significance from granite bodies in Tangzhangzi and Niuxinshan, eastern Hebei Province, China. *Geol. Bull. China* **2009**, *28*, 1458–1464. (In Chinese)
22. Zhang, J.G.; Shao, Y.J.; Wang, C.; Liu, Z.F.; Xiong, Y.Q. Characteristics of gold-bearing minerals in Xiajinbao gold deposit of Hebei and their metallogenic indicating significance. *J. Cent. South Univ.* **2018**, *49*, 901–909. (In Chinese)
23. Zhou, L.G.; Xia, Q.X.; Zheng, Y.F.; Hu, Z.C. Poly-phase growth of garnet in eclogite from the Hong'an orogen: Constraints from garnet zoning and phase equilibrium. *Lithos* **2014**, *206–207*, 79–99. [[CrossRef](#)]
24. Liu, Y.S.; Gao, S.; Hu, Z.C.; Gao, C.G.; Zong, K.Q.; Wang, D. Continental and oceanic crust recycling-induced melt–peridotite interactions in the Trans-North China Orogen: U–Pb dating, Hf isotopes and trace elements in zircons from mantle xenoliths. *J. Petrol.* **2010**, *51*, 537–571. [[CrossRef](#)]
25. Hou, K.J.; Li, Y.H.; Zou, T.R.; Qu, X.M.; Shi, Y.R.; Xie, G.Q. Laser ablation–MC–ICP–MS technique for Hf isotope microanalysis of zircon and its geological applications. *Acta Petrol. Sin.* **2007**, *23*, 2595–2604. (In Chinese)
26. Elhlou, S.; Belousova, E.; Griffin, W.L.; Pearson, N.J.; O'reilly, S.Y. Trace element and isotopic composition of GJ-red zircon standard by laser ablation. *Geochim. Cosmochim. Acta* **2006**, *70*, 158. [[CrossRef](#)]
27. Liu, Q.Q.; Li, B.; Shao, Y.J.; Lu, A.H.; Lai, J.Q.; Li, Y.F.; Luo, Z.C. Molybdenum mineralization related to the Yangtze's lower crust and differentiation in the Dabie Orogen: Evidence from the geochemical features of the Yaochong porphyry Mo deposit. *Lithos* **2017**, *282/283*, 111–127. [[CrossRef](#)]
28. Chappell, B.W.; White, A.J.R. I- and S-type granites in the Lachlan fold belt. *Earth Sci.* **1992**, *83*, 1–26.
29. Belousova, E.A.; Griffin, W.L.; O'Reilly, S.Y.; Fisher, N.L. Igneous zircon: Trace element composition as an indicator of source rock type. *Contrib. Mineral. Petrol.* **2002**, *143*, 602–622. [[CrossRef](#)]
30. Hoskin, P.W.O.; Schaltegger, U. The composition of zircon and igneous metamorphic petrogenesis. *Rev. Mineral. Geochem.* **2003**, *53*, 27–62. [[CrossRef](#)]
31. Clayton, R.N.; O'Neil, J.R.; Mayeda, T.K. Oxygen isotope exchange between quartz and water. *J. Geophys. Res.* **1972**, *77*, 3057–3067. [[CrossRef](#)]
32. Luo, Z.K.; Qiu, Y.S.; Guan, K.; Miao, L.C.; Qiu, Y.M.; McNaughton, N.J.; Groves, D.I. SHRIMP U–Pb dating on zircon from Yu'erya and Niuxinshan granite intrusions in eastern Hebei province. *Bull. Mineral. Petrol. Geochem.* **2001**, *20*, 278–285.
33. Chen, S.C.; Ye, H.S.; Wang, Y.T.; Zhang, X.K.; Lu, D.Y.; Hu, H.B. Re–Os age of molybdenite from the Yuerya Au deposit in eastern Hebei Province and its geological significance. *Geol. China* **2014**, *41*, 1565–1576. (In Chinese)
34. Li, Z.Y.; Ye, H.S.; He, W.; Cao, J.; Zhang, X.K.; Wang, S.; Lu, D.Y.; Li, C. Geological characteristics and molybdenite Re–Os isotopic dating of Tangzhangzi gold (molybdenum) deposit in eastern Hebei Province. *Miner. Depos.* **2014**, *33*, 1366–1378. (In Chinese)
35. Hu, D.X. *Gold-Bearing Quartz vein ⁴⁰Ar–³⁹Ar Age at the Margin of the North China Craton*; China University of Geosciences Press: Beijing, China, 1996; pp. 1–100. (In Chinese)
36. Bea, F.; Arzamastsev, A.; Montero, P.; Arzamastseva, L. Anomalous alkaline rocks of Soustov, Kola: Evidence of mantle-derived metasomatic fluids affecting crustal materials. *Contrib. Mineral. Petrol.* **2001**, *140*, 554–566. [[CrossRef](#)]
37. Zheng, W.; Mao, J.W.; Zhao, H.J.; Zhao, C.S.; Yu, X.F. Two Late Cretaceous A-type granites related to the Yingwuling W–Sn polymetallic mineralization in Guangdong province, South China: Implications for petrogenesis, geodynamic setting, and mineralization. *Lithos* **2017**, *274/275*, 106–122. [[CrossRef](#)]
38. Sylvester, P.J. Post-collisional strongly peraluminous granites. *Lithos* **1998**, *45*, 29–44. [[CrossRef](#)]
39. Xu, X.Y.; Jiang, N.; Fan, W.B.; Hu, J.; Zong, K.Q. Petrogenesis and geological implications for the Mesozoic granites in Qinglong area, eastern Hebei province. *Acta Petrol. Sin.* **2016**, *32*, 212–232. (In Chinese)
40. Zartman, R.E.; Doe, B.R. Plumbotectonics—The model. *Tectonophysics* **1981**, *75*, 135–162. [[CrossRef](#)]
41. Shi, C.L.; Song, Y.; Hu, J.Z.; Zhao, B.; Wang, T.; Liao, Y.Z. Characteristics and geological significance of stable isotopes in the Huajian gold deposit, Hebei province. *Bull. Mineral. Petrol. Geochem.* **2015**, *34*, 362–368. (In Chinese)

42. Xin, C.L.; Gong, X.; Zhu, X.L.; Zhao, Z.P. Geological characteristics and genesis of Dongliang gold deposit in eastern Hebei province. *Contrib. Geol. Miner. Resour. Res.* **2014**, *29*, 51–58. (In Chinese)
43. Lin, E.W.; Guo, Y.J. Lead isotope studies on goldfields in eastern, Hebei, China. *J. Jilin Univ.* **1985**, *1*, 1–10. (In Chinese)
44. Chappell, B.W. Aluminium saturation in I- and S-type granites and the characterization of fractionated haplogranites. *Lithos* **1999**, *46*, 535–551. [[CrossRef](#)]
45. Chappell, B.W.; White, A.J.K. Two contrasting granite types. *Pac. Geol.* **1974**, *8*, 173–174.
46. Frost, C.D.; Frost, B.R. Reduced rapakivi type granites: The tholeiitic connection. *Geology* **1997**, *25*, 647–650. [[CrossRef](#)]
47. Whalen, J.B.; Currie, K.L.; Chappell, B.W. A-type granites: Geochemical characteristics, discrimination and petrogenesis. *Contrib. Mineral. Petrol.* **1987**, *95*, 407–419. [[CrossRef](#)]
48. Li, H.B.; Shao, Y.J.; Liu, Z.F.; Zhang, Y.; Wei, H.T.; Wang, C. Geochemical characteristics of ore-bodies in Xiajinbao Au deposit in Pingquan of Hebei and its relationship with mineralization. *Miner. Resour. Geol.* **2014**, *28*, 356–360. (In Chinese)
49. Münker, C.; Wörner, G.; Yogodzinski, G.; Churikova, T. Behavior of high field strength elements in subduction zones: Constraints from Kamchatka–Aleutian arc lavas. *Earth Planet. Sci. Lett.* **2004**, *224*, 275–293. [[CrossRef](#)]
50. Bau, M. Controls on the fractionation of isovalent trace elements in magmatic and aqueous systems: Evidence from Y/Ho, Zr/Hf, and lanthanide tetrad effect. *Contrib. Mineral. Petrol.* **1996**, *123*, 323–333. [[CrossRef](#)]
51. Zhao, K.D.; Jiang, S.Y. Rare earth element and yttrium analyses of sulfides from the Dachang Sn-polymetallic ore field, Guangxi Province, China: Implication for ore genesis. *Geochem. J.* **2007**, *41*, 121–134. [[CrossRef](#)]
52. Li, X.H.; Liu, Y.; Yang, Y.H.; Chen, F.K.; Tu, X.L.; Qi, C.S. Rapid separation of Lu–Hf and Sm–Nd from a single rock dissolution and precise measurement of Hf–Nd isotopic ratios for national rock standards. *Acta Petrol. Sin.* **2007**, *23*, 221–226. (In Chinese)
53. Sheppard, S.M.F. Characterization and isotopic variations in natural waters. *Rev. Mineral. Geochem.* **1986**, *16*, 165–183.
54. Wang, T. Study on the Ore-Forming Geological Process in Niuxinshan Section of Hebei Huajian Gold Deposit. Master’s Thesis, China University of Geosciences, Beijing, China, 2012. (In Chinese)
55. Zhang, Q.S.; Yang, Z.S.; Gao, D.Y. *Jidong Jinchangyu Regional High-Grade Metamorphic Geology and Gold Deposits*; Geological Publishing House: Beijing, China, 1991; pp. 1–445. (In Chinese)
56. Jie, B. The Geochemical Characteristic and the Ore-Forming Material Source of Yuerya Gold Mine in Hebei Province. Master’s Thesis, China University of Geosciences, Beijing, China, 2013. (In Chinese)
57. He, W. The Study of Geology, Geochemical and Mineralization of Tangzhangzi Au Polymetallic Deposit, East Hebei Province. Master’s Thesis, China University of Geosciences, Beijing, China, 2015. (In Chinese)
58. Ohmoto, H. Systematics of sulfur and carbon isotopes in hydrothermal ore deposits. *Econ. Geol.* **1972**, *67*, 551–578. [[CrossRef](#)]
59. Ohmoto, H.; Rye, R.O. Isotope of sulfur and carbon. In *Geochemistry of Hydrothermal Ore Deposits*, 2nd ed.; Barnes, H.I., Ed.; John Wiley and Sons: New York, NY, USA, 1979; pp. 509–561.
60. Chaussidon, M.; Albarède, F.; Sheppard, S.M.F. Sulphur isotope variation in the mantle from microprobe analysis of micro-sulphide inclusion. *Earth Planet. Sci. Lett.* **1989**, *92*, 144–156. [[CrossRef](#)]
61. Peng, J.T.; Hu, R.Z.; Su, W.C. Lead isotopic composition of ores in the antimony deposits at the southern margin of the Yangtze massif and its geological implication. *Geol. Geochem.* **2000**, *28*, 43–47. (In Chinese)
62. Windley, B.F.; Maruyama, S.; Xiao, W.J. Delamination/thinning of sub-continental lithospheric mantle under Eastern China: The role of water and multiple subduction. *Am. J. Sci.* **2010**, *310*, 1250–1293. [[CrossRef](#)]
63. Tang, Y.J.; Zhang, H.F.; Santosh, M.; Ying, J.F. Differential destruction of the North China Craton: A tectonic perspective. *J. Asian Earth Sci.* **2013**, *78*, 71–82. [[CrossRef](#)]
64. Dong, S.W.; Zhang, Y.Q.; Long, C.X.; Yang, Z.Y.; Ji, Q.; Wang, T.; Hu, J.M.; Chen, X.H. Jurassic tectonic revolution in China and new interpretation of the Yanshan movement. *Acta Geol. Sin.* **2007**, *81*, 1449–1461. (In Chinese)
65. Tomurtogoo, O.; Windley, B.F.; Kroner, A. Zircon age and occurrence of the Adaatsag ophiolite and Muron shear zone, central Mongolia: Constraints on the evolution of the Mongol–Okhotsk Ocean, suture and orogen. *J. Geol. Soc.* **2005**, *162*, 125–134. [[CrossRef](#)]
66. Zorin, Y.A. Geodynamics of the western part of the Mongolia–Okhotsk collisional belt, Trans-Baikal region (Russia) and Mongolia. *Tectonophysics* **1999**, *306*, 33–56. [[CrossRef](#)]

67. Wu, F.Y.; Yang, J.H.; Lo, C.H. The Heilongjiang group: A Jurassic accretionary complex in the Jiamusi massif at the western Pacific margin of northeastern China. *Island Arc* **2007**, *16*, 156–172. [[CrossRef](#)]
68. Isozaki, Y. Jurassic accretion tectonics of Japan. *Island Arc* **1997**, *6*, 25–51. [[CrossRef](#)]
69. Maruyama, S.; Isozaki, Y.; Kimura, G.; Terabayashi, M. Paleogeographic maps of the Japanese Islands: Plate tectonic synthesis from 750 Ma to the present. *Island Arc* **1997**, *6*, 121–142. [[CrossRef](#)]
70. Kojima, S.; Kemlin, I.V.; Kametaka, M. A correlation of accretionary complexes of southern Sikhote-Alin of Russia and the Inner Zone of Southwest Japan. *Geosci. J.* **2000**, *4*, 175–185. [[CrossRef](#)]
71. Burnham, C.W.; Ohmoto, H. Late-stage processes of felsic magmatism. *Soc. Min. Geol. Jpn.* **1980**, *8*, 1–11.
72. Hayashi, K.; Ohmoto, H. Solubility of gold in NaCl and H₂S-bearing aqueous solutions at 250 °C–350 °C. *Geochim. Cosmochim. Acta* **1991**, *55*, 2111–2126. [[CrossRef](#)]
73. Cole, D.R.; Drummond, S.E. The effect of transport and boiling on Ag/Au ratios in hydrothermal solutions: A prelim in ray assessment and possible implications for the formation of epithermal precious metal ore deposits. *Geochem. Explor.* **1986**, *25*, 45–79. [[CrossRef](#)]
74. Zhang, D.H. Some new advances in ore-forming fluid geochemistry on boiling and mixing of fluid during the processes of hydrothermal deposits. *Adv. Earth Sci.* **1997**, *12*, 546–552. (In Chinese)
75. Xu, G.F.; Shao, J.L. On the study of the typomorphism of minerals in the applications of approaching gold deposits genesis and prospection. *Gansu Geol.* **1984**, *6*, 1–19. (In Chinese)
76. Thompson, J.F.H.; Sillitoe, R.H.; Baker, T.; Lang, J.R.; Mortensen, J.K. Intrusion-related gold deposits associated with tungsten-tin provinces. *Mineral. Depos.* **1999**, *34*, 323–334. [[CrossRef](#)]
77. Sillitoe, R.H. Gold-rich porphyry deposits: Descriptive and genetic models and their role in exploration and discovery. *Rev. Econ. Geol.* **2000**, *13*, 315–345.
78. Lang, J.R.; Baker, T.; Hart, C.J.R.; Mortensen, J.K. An exploration model for intrusion-related gold systems. *Soc. Econ. Geol. Newsl.* **2000**, *40*, 1, 6–15.
79. Blevin, P.L.; Chappell, B.W.; Allen, C.M. Intrusive metallogenic provinces in eastern Australia based on granite source and composition. Transactions of the Royal Society of Edinburgh. *Earth Sci.* **1996**, *87*, 281–290.
80. Baker, T.; Pollard, P.J.; Mustard, R.; Graham, J.L. A comparison of granite-related tin, tungsten, and gold-bismuth deposits: Implications for exploration. *Soc. Econ. Geol. Newsl.* **2005**, *61*, 5–17.
81. Li, H.B.; Ishiyama, D.; Zhang, Y.; Shao, Y.J. Geology and geochemical characteristics of the Xiajinbao gold deposit in the Hebei Province, China. *J. Mineral. Petrol. Sci.* **2018**, *113*, 24–40. [[CrossRef](#)]
82. Mitchell, A.H.G.; Garson, M.S. *Mineral Deposits and Global Tectonic Settings*; Academic Press: London, UK, 1981; 405p.
83. Sawkins, F.J. *Metal Deposits in Relation to Plate Tectonics*; Springer: Berlin, Germany, 1984; 325p.
84. Duuring, P.; Cassidy, K.F.; Hagemann, S.G. Granitoid-associated orogenic, intrusion-related, and porphyry style metal deposits in the Archean Yilgarn craton, Western Australia. *Ore Geol. Rev.* **2007**, *32*, 157–186. [[CrossRef](#)]
85. Khashgerel, B.E.; Kavalieris, I.; Hayashi, K.I. Mineralogy, textures, and whole-rock geochemistry of advanced argillic alteration: Hugo Dummett porphyry Cu–Au deposit, Oyutolgoi mineral district, Mongolia. *Mineral. Depos.* **2008**, *43*, 913–932. [[CrossRef](#)]
86. Sillitoe, R.H.; Thompson, J.F.H. Intrusion-related vein gold deposits: Types, tectono-magmatic settings and difficulties of distinction from orogenic gold deposits. *Resour. Geol.* **1998**, *48*, 237–250. [[CrossRef](#)]
87. Mair, J.L.; Hart, C.J.R.; Goldfarb, R.J.; O’Dea, M.; Harris, S. Geology and metallogenic signature of gold occurrences at Scheelite Dome, Tombstone gold belt, Yukon. In *Yukon Exploration and Geology 1999*; Emond, D.S., Westen, L.H., Eds.; Exploration and Geological Services Division, Yukon, Indian and Northern Affairs Canada: Whitehorse, YT, Canada, 2000; pp. 165–176.
88. Jia, S.S.; Wang, E.D.; Fu, J.F.; Guo, Y.Y. Ore-forming geological characteristics, geochemistry and formation mechanism of Jinchangyu gold deposit in eastern Hebei province. *J. Jilin Univ.* **2012**, *33*, 1492–1494. (In Chinese)
89. Xiao, W.J.; Windley, B.F.; Hao, J.; Zhai, M.G. Accretion leading to collision and the Permian Solonker suture, Inner Mongolia, China: Termination of the central Asian orogenic belt. *Tectonics* **2003**, *22*, 1–21. [[CrossRef](#)]
90. Jian, P.; Lui, D.; Kröner, A.; Windley, B.F.; Shi, Y.; Zhang, W.; Zhang, F.; Miao, L.; Zhang, L.; Tomurhuu, D. Evolution of a Permian intraoceanic arc–trench system in the Solonker suture zone, Central Asian Orogenic Belt, China and Mongolia. *Lithos* **2010**, *118*, 169–190. [[CrossRef](#)]

91. Ma, Q. *Triassic–Jurassic Volcanic Rocks in Western Liaoning: Implications for Lower Crustal Reworking and Lithospheric Destruction in the North Part of Eastern North China Craton*; China University of Geosciences: Wuhan, China, 2013. (In Chinese)
92. Zhu, X.L. *Geological Characteristics and Genesis of Dongliang Gold Deposit in Eastern Hebei*; Northwest Normal University: Lanzhou, China, 2014. (In Chinese)



© 2018 by the authors. Licensee MDPI, Basel, Switzerland. This article is an open access article distributed under the terms and conditions of the Creative Commons Attribution (CC BY) license (<http://creativecommons.org/licenses/by/4.0/>).